International Journal of Nanomedicine

Dovepress
open access to scientific and medical research

Open Access Full Text Article

ORIGINAL RESEARCH

Multifunctional Nanoparticles-Mediated PTT/PDT Synergistic Immune Activation and Antitumor Activity Combined with Anti-PD-L1 Immunotherapy for Breast Cancer Treatment

Cunqing Kong[1,*], Banghao Xu[2,*], Guanhua Qiu[1], Meng Wei[2], Mengqi Zhang[3], Shengxian Bao[1], Jiali Tang[1], Lequn Li[2], JunJie Liu[1]

[1]Department of Ultrasound, Affiliated Tumor Hospital of Guangxi Medical University, Nanning, 530021, People's Republic of China; [2]Department of Hepatobiliary Surgery, Affiliated Tumor Hospital of Guangxi Medical University, Nanning, 530021, People's Republic of China; [3]Department of Interventional Therapy Affiliated Tumor Hospital of Guangxi Medical University, Nanning, 530021, People's Republic of China

*These authors contributed equally to this work

Correspondence: JunJie Liu, Department of ultrasound, Affiliated Tumor Hospital of Guangxi Medical University, 71 Hedi Road, Nanning, 530021, People's Republic of China, Email liujunjie@gxmu.edu.cn; Lequn Li, Department of hepatobiliary surgery, Affiliated Tumor Hospital of Guangxi Medical University, 71 Hedi Road, Nanning, 530021, People's Republic of China, Email li_lequn@263.net

Introduction: Photoimmunotherapy is a breakthrough treatment for malignant tumors. Its uniqueness is that it uses antibody mediated targeted delivery to achieve high tumor specificity and uses laser-activated biophysical mechanism to accurately induce the rapid death of cancer cells and avoid damaging the surrounding normal tissues.

Methods: In this paper, an iron-based micelle was designed to encapsulate the photothermal agent indocyanine green (ICG) and a cyclic tripeptide of arginine-glycine-aspartic acid (cRGD) as targeted multifunctional ICG@SANPs-cRGD nanoparticles for combined photothermal/photodynamic/immune therapy of breast cancer.

Results: The experimental results show that ICG@SANPs-cRGD nanoparticles have good biocompatibility and photothermal conversion ability. Photothermal therapy (PTT) and photodynamic therapy (PDT) based on ICG@SANPs-cRGD can not only inhibit the proliferation, invasion and migration of tumor cells, but also directly kill tumor cells by inducing apoptosis or necrosis. Dual-mode fluorescence light (FL) and magnetic resonance imaging (MRI) imaging in mice confirmed the selective accumulation at tumor sites and imaging ability of ICG@SANPs-cRGD. PTT/PDT combined with Anti-PD-L1 immunotherapy based on ICG@SANPs-cRGD mediated the immunogenic cell death (ICD) of tumor cells by regulating the expression of immune-related indicators and activated the body's immune response mechanism, which enhanced the immunotherapy effect of immune checkpoint block (ICB). PTT/PDT combined with Anti-PD-L1 therapy not only prevented the progression of the primary tumor but also inhibited the distant metastasis of the tumor.

Discussion: This study explores the biomedical application of PTT/PDT combined with Anti-PD-L1 based on ICG@SANPs-cRGD nanomaterials for breast cancer treatment and demonstrates the potential of ICG@SANPs-cRGD as a multifunctional therapeutic platform for future cancer therapy.

Keywords: photodynamic therapy, photothermal therapy, immune checkpoint blocking, immune enhancement effect

Introduction

Cancer is a major public health problem worldwide and the second leading cause of death in the United States. More than 600,000 Americans die of cancer in 2020, equivalent to an estimated 16 million deaths, among them, breast cancer is estimated to be the second leading cause of death in women with an estimated 276,000 new cases each year in the United States.[1] Currently, the treatment of breast cancer mainly includes surgery, radiotherapy, chemotherapy, endocrine therapy and biological therapy, etc., but each treatment has various limitations, such as high aggressiveness, unsatisfactory

Received: 4 May 2022
Accepted: 8 November 2022
Published: 17 November 2022

therapeutic effect, inevitable toxic and side effects caused by lack of tumor specificity, and the risk of tumor recurrence.[2–4] Therefore, the treatment situation of breast cancer is not optimistic, and the development of new and more effective treatment methods is imminent. At present, some new therapies for cancer treatment, such as immunotherapy, gene therapy, phototherapy and magnetic thermotherapy, etc, have been gradually reported, and some of them have also been applied in preclinical research. It should be noted that near-infrared ray (NIR)-mediated PTT and PDT have attracted more and more attention in tumor treatment.[5,6] PTT mainly converts light energy into heat energy under the irradiation of NIR through the action of photothermal agent (PTA), which can quickly and effectively kill tumor cells or tissues.[7–11]

However, PTT can also lead to uneven heat distribution in tumor tissue due to light attenuation or uneven distribution of photosensitizers, which weakens the therapeutic effect of PTT. In addition, the high temperature caused by PTT may also damage normal tissue.[12,13] The photosensitizer reacts with molecular oxygen under the irradiation of PDT-specific wavelength laser to generate effective singlet oxygen. Singlet oxygen damages tumor cells and blood vessels through apoptosis, necrosis, and activation of immune responses,[14,15] but the severe hypoxic environment of tumors limits its therapeutic effect.[16] Therefore, single PTT/PDT treatment has inherent deficiencies, so synergistic PTT/PDT is a good choice, because the heat generated by PTT can increase blood flow and improve intratumor oxygen supply, thus improving the therapeutic effect of PDT.[17] In addition, PDT can also increase the sensitivity of PTT by altering the tumor microenvironment (TME) and interfering with tumor physiology.[18] However, the depth of light tissue penetration of NIR has become a major obstacle to the effect of phototherapy. It can be seen that phototherapy itself is not enough to completely eliminate tumors.[19] Therefore, the combination of phototherapy and immunotherapy may bring ideal anticancer effects.

The advantages of immunotherapy in cancer treatment have become increasingly prominent, and more and more results have shown that immune checkpoint mechanisms play an important role in suppressing antitumor T cell-mediated immune responses in TEM.[20] Studies have shown that programmed cell death 1 (PD-1) and its major ligand programmed cell death ligand 1 (PD-L1) signaling pathway is a key immune checkpoint and that inhibition using monoclonal antibodies can reverse T cell function handicap or exhaustion.[21] PD-1/PD-L1 blockade has achieved remarkable results in the clinical treatment of many different malignancies such as colorectal cancer,[22] breast cancer,[23] bladder cancer[24] and non-small cell lung cancer (NSCLC),[25] especially, when combined with other therapies, the anti-tumor effect was significantly enhanced. Therefore, in this study, we designed a multifunctional nanoparticle ICG@SANPs-cRGD coated with photosensitifier ICG and surface modified cRGD using iron-based micelles as a carrier, which can enhance the anti-tumor effect of PTT/PDT combined with Anti-PD-L1 immunotherapy (Scheme 1).

Materials and Methods

Synthesis of ICG@SANPs and ICG@SANPs-cRGD Nanoparticles

Fe_3O_4 ferrite SANPs coated with oleic acid (OA) (Aladdin, Shanghai, China) and dimercaptosuccinic acid (DMSA) were synthesized by thermal decomposition method. Then, SANPs coated with OA (15mg, iron content) and DSPE-PEG2000-COOH (1,2-Distearoyl-Sn-glycero-3-phosphoethanolamine-N-[carboxy (polyethylene)]) powder, >98% (purchased from Shanghai A.V.T. Pharmaceutical Ltd, China) (100mg), mixed together and poured into a 25mL round-bottom flask with 10mL chloroform. Then, 5mL deionized water was added to the flask. The chloroform was slowly evaporated at 65°C for 20 minutes. After complete evaporation, water-soluble SANPs containing PEG were obtained.

Activate the-COOH group on the surface of DSPE-PEG2000-COOH in SANPs containing PEG,1-ethyl-3-(dimethylaminopropyl) carbodiimide Hydro-chloride (EDC, 100mg) (Aladdin, Shanghai, China) and N-hydroxysuccinimide (NHS, 90mg) (Aladdin, Shanghai, China) were added to 20mL 2-(N-morpholino) ethanesulfonic acid buffer (MES, 0.02mol/L, PH 5~5.5) and stirred and cultured at room temperature for 20 minutes. Ultracentrifugation (100,000g), washed twice with deionized water, the active intermediate was dispersed in borate buffer (0.02 mol/L), 10mg cyclic RGD was slowly added and stirred continuously for 24h at room temperature. The SANPs@RGD obtained by concentration was washed 3 times with deionized water, and excess empty lipid micelles were removed from the deposited SANPs by supercentrifugation (100,000g). Finally, the purified SANPs@RGD was centrifuged at 3000g, and then the large aggregates were discarded, thereby obtaining the SANPs@RGD.

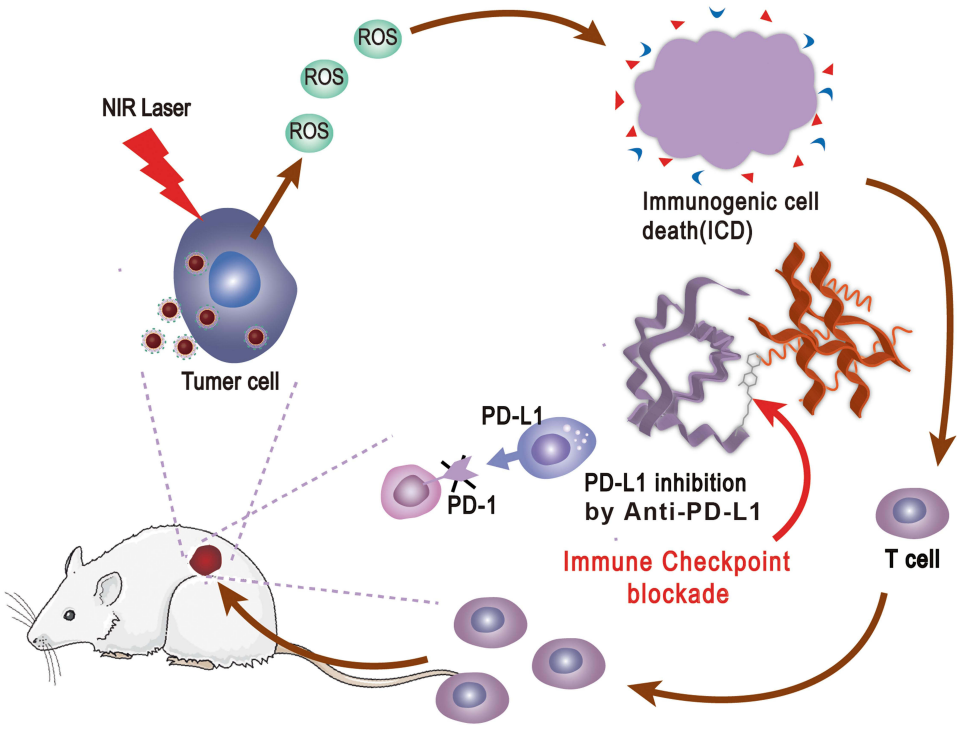

Scheme 1 Design principle of ICG@SANPs-cRGD nanoparticles for enhanced PTT/PDT combined with Anti-PD-L1 immunotherapy.

Finally, the photosensitizer ICG (HWRK CHEM, Beijing, China) was loaded into the above-synthesized PEG-containing SANPs and SANPs@RGD, respectively, as a tricarbocyanine dye. 1mL of ICG aqueous solution with a concentration of 1mg/mL was added to the two compositions, placed on a shaker at room temperature overnight, and then ultracentrifuged (100,000g) to remove unloaded ICG molecules to obtain the ICG@SANPs and ICG@SANPs-cRGD nanoparticles required for the experiment.

Characterization of ICG@SANPs-cRGD Nanoparticles

The size, shape and dispersion of ICG@SANPs-cRGD were determined by transmission electron microscopy (TEM) (JEOL-2100F, Japan). The hydrodynamic size and zeta potential of nanoparticles were measured by Zetasizer Nano ZS90 (Malvern, UK) by dynamic light scattering (DLS). The UV-vis-NIR absorption spectrum was obtained on a UV-2600 UV-Vis-NIR spectrophotometer (185–900nm, Jiangsu, China). A PPMS-9 Vibrating Sample Magnetometer (VSM) (Quantum Design, USA) was used to measure the specific saturation magnetization and coercivity of ICG@SANPs-cRGD at room temperature.

MRI Imaging of ICG@SANPs-cRGD Nanoparticles in vitro

The different concentrations of ICG@SANPs-cRGD solution (0μg/mL, 1μg/mL, 5μg/mL, 10μg/mL, 25μg/mL, 50μg/mL) was placed in eppendorf tubes (1.5mL) and vortexed for 3 min, respectively. T1-weighted MRI images were acquired using a 3.0T magnetic resonance imaging scanner (MRI) (Discovery MR750, GE Healthcare, USA). The scanning parameters were set as follows: T1WI: FOV 80cm × 80cm, slice thickness 2mm, slice spacing 0.2mm, matrix 256 × 256, TR 825ms, TE 11.5ms. The images of T1WI were analyzed and processed on GE ADW4.6 workstation.

Biocompatibility Detection of ICG@SANPs-cRGD Nanoparticles

BALB/c mice (female, 6–8 weeks old, body weight 20 ± 2g) were collected from Guangzhou Yancheng Biotechnology Co., LTD. (Guangzhou, China) and managed by Guangxi Medical University (Guangxi Experimental Animal Center). All animal experiments have been approved by The Experimental Animal Welfare and Ethics Committee of Guangxi

Medical University. All animal experiments followed The National Standard of the People's Republic of China GB/T35892-2018 "Guidelines for Ethical Review of Laboratory Animal Welfare". After the mice were anesthetized, 100μL of fresh blood was taken from the heart and placed in an EDTA anticoagulant tube, centrifuged at 3000rpm for 5min to remove the upper plasma, then washed with PBS three times for red blood cells, and finally resuspended the red blood cell pellet with 4 mL of PBS. Then, 10μL of ICG@SANPs-cRGD solutions with different concentrations (10μg/mL, 20μg/mL, 40μg/mL, 60μg/mL, 80μg/mL, 100μg/mL) were taken, PBS was the negative control, and ionized water was the positive control. About 900μL of red blood cell suspension was mixed gently, and then the centrifuge tube was placed in a water bath in a 37°C incubator. After incubation for 8 hours, the supernatant was centrifuged to measure the absorbance (wavelength set at 570nm).

The calculation formula of hemolysis percentage is as follows: hemolysis (%) = $(I–I_{PBS})/(I_0-I_{PBS}) \times 100\%$, where I is the absorbance of hemoglobin with different concentrations of ICG@SANPs-cRGD nanoparticles, I_{PBS} is the absorbance of hemoglobin in PBS, and I_0 represents complete hemolysis in ionic water.

Detection of Cellular Internalization Ability of ICG@SANPs-cRGD Nanoparticles

2×10^5 4T1 cells (purchased from Hanyin Biotechnology Co., Ltd.) were seeded on a special culture dish for confocal laser (CLSM) (Diameter/size: 35mm/15mm, Catalog No. 801002, Nestle Biotechnology Co., Ltd., Wuxi, China), and cultured in a cell incubator under normal conditions (37°C, 5% CO2, 95% humidity), when the cell density reached 70–80%, the original medium was discarded, and 10 μL of ICG@SANPs-cRGD and ICG@SANPs were added to incubate for 1 h, and then the liquid was discarded, washed twice with PBS, 10μg/mL Hoechst 33342 Staining Solution (1mg/mL, Solarbio Technology Co., Ltd. Beijing, China) was added into each dish. After staining for 5min, PBS buffer was used to clean the stain for 3 times under dark conditions, 5min each time. The uptake of ICG@SANPs-cRGD and ICG@SANPs by 4T1 cells was observed under a confocal laser scanning microscope (CLSM) (Leica TCS SP8, Germany) with an excitation wavelength of 750 nm and an emission wavelength of 817nm.

Evaluation of the Biocompatibility of ICG@SANPs-cRGD Nanoparticles in vitro

1×10^4 cells/well of healthy mouse fibroblast cell line (L929) and alpha mouse liver 12 (AML-12) cells (obtained from the Cell Bank of Shanghai Institute of Biochemistry and Cell Biology, Chinese Academy of Sciences) were inoculated in 96-well plates and incubated overnight in an incubator.

The medium was then changed to fresh medium containing different concentrations of ICG@SANPs-cRGD (0μg/mL, 10μg/mL, 20μg/mL, 40μg/mL, 60μg/mL, 80μg/mL and 100μg/mL). After 24 hours, the original medium was discarded, and 100μL of 10% CCK-8 FBS medium was added to each well. After 2h, live cells were detected by CCK8 assay kit (Beyotime Biotechnology, Shanghai, China). The optical density (OD) at 450nm was measured with a multi-function microplate reader (Thermo, USA), and the cell viability = $(OD_{sample}-OD_{blank})/(OD_{control}-OD_{blank}) \times 100\%$ was calculated. The cytotoxicity of nanoparticles is reflected by cell viability.

Photothermal Properties of ICG@SANPs-cRGD Nanoparticles in vitro

ICG@SANPs-cRGD solutions with concentrations of 0μg/mL, 5μg/mL, 10μg/mL, 15μg/mL and 20μg/mL were placed in 6-well plates, and then irradiated with near-infrared light with a wavelength of 808nm (BWT, Beijing, China) irradiated for 10min, the power density was $0.8W/cm^2$. In addition, the concentration of ICG@SANPs-cRGD solution was diluted to 10μg/mL and then irradiated with different power densities of $0.4W/cm^2$, $0.8W/cm^2$ and $1.2W/cm^2$ for 10min, respectively. Infrared thermal phase forming thermal imager (HIKVISION, Hangzhou, China) is used to record the temperature changes of ICG@SANPs-cRGD solution at different concentrations and different powers every 30s.

Detection of ROS Generation

2×10^5 cells/well of 4T1 cells were seeded in 6-well plates, and after 24 hours of culture, the 6 groups (same as above) were mixed with 1mL of 2', 7'-dichlorofluorescein diacetate (DCFH-DA) (Beyotime Biotechnology, Shanghai, China) was incubated with FBS-free medium for 20 minutes, after 4h, the level of intracellular reactive oxygen species (ROS)

was evaluated by detecting the fluorescence of DCF with inverted fluorescence microscope (Zeiss, LSM510, Shanghai, China). The 808nm laser irradiation (0.8w/cm^2, 3min) was still carried out under dark environment.

Proliferation Experiment in vitro

1×10^4 cells/well of 4T1 cells were seeded in a 96-well plate, after culturing for 24 hours, the cells were subjected to the following 6 different treatments: NC, NIR, ICG@SANPs, ICG@SANPs-cRGD, NIR+ICG@SANPs, NIR +ICG@SANPs-cRGD. Among them, NIR, NIR+ICG@SANPs and NIR+ICG@SANPs-cRGD were irradiated with 808nm laser (0.8W/cm^2, 3min) under dark conditions, continued to culture for 24h, and then discarded the original medium, all wells were washed three times with PBS, and 100μL of FBS medium containing 10% CCK-8 was added to each well. Two hours later, the optical density was measured at 450nm with multifunctional microplate analyzer, and the cell proliferation rate was calculated.

The same method was used to observe the effects of different concentrations of ICG@SANPs-cRGD solutions (0μg/mL, 2.5μg/mL, 5μg/mL, 10μg/mL, 20μg/mL, 25μg/mL) on the viability of 4T1 cells under irradiation at 808nm (0.8W/cm^2, 3min), and the effect of the same ICG@SANPs-cRGD solution concentration (10μg/mL) on the viability of 4T1 cells at different culture time points (2h, 4h, 8h, 16h, 24h).

In vitro Cloning Experiment

5×10^3 cells/well of 4T1 were seeded in a 6-well plate, after 24 hours, 6 groups (same as above) were performed with different treatments, the concentration of nanoparticles was 10μg/mL. Two hours later, the irradiation group was irradiated with 808nm NIR (0.8W/cm^2, 3min) under dark conditions and cultured in medium containing 10% FBS for approximately 14 days, and the medium was changed every 2 days. It was fixed with methanol (Sinopharm Chemical Reagent Co., Ltd, Shanghai, China) and stained with 0.1% Crystal violet (Article Number: C8470-25g, Solarbio, Beijing, China). Colony formation was assessed by counting the number of stained colonies.

Cell Death Status Was Detected by Calcein-AM/PI Double Staining

4T1 cells at logarithmic growth stage were prepared into 1×10^5/mL single-cell suspension, which was inoculated in 6-well plates and cultured in a cell incubator under normal conditions for 24h; then treated with six groups of different treatments (same as above), the concentration of nanoparticles was 10μg/mL, and continued to culture for 2h, then, the group that needed irradiation was taken out with infrared ray with wavelength of 808nm and illuminated for 3min with power density of 0.8W/cm^2 under the condition of light avoidance. Then, it was put back into the cell culture box for 24h and cleaned once with 1×PBS buffer solution. One milliliter of Calcein-AM/PI was added to each well to detect the working fluid (Beyotime Biotechnology, Shanghai, China). After incubation at 37°C for 30min, fluorescence was observed and photographed under a fluorescence microscope (Calcein-AM green fluorescence Ex/Em = 494/517nm; PI is red fluorescence, Ex/Em = 535/617nm).

Detection of Photothermal Effect in vivo

When the tumor volume of the constructed 4T1 breast cancer BALB/c mice reached 100mm^3, the mice were randomly divided into three groups (n = 4): PBS, ICG@SANPs, ICG@SANPs-cRGD, three kinds of solutions (1mg/mL, 100μL) were injected into the tail vein of mice. After 4h, the tumor sites of the three groups were exposed to 808nm laser (0.8W/cm^2, 3min), and the temperature changes of tumor sites were recorded by infrared thermal imager.

Fluorescence Imaging in vivo

About 100μL of 4T1 cell suspension (1×10^6) was injected subcutaneously into the back side of BALB/C mice to construct 4T1 tumor-bearing mouse model. When the tumor volume of 4T1 tumor-bearing mice reached 100mm^3, ICG@SANPs-cRGD and ICG@SANPs were injected into the mice through tail vein injection within the safe dose range, the tumor was irradiated with NIR at different time points (0h, 1h, 2h, 3h, 4h, 5h and 6h). After irradiation, the mice under anesthesia were scanned by IVIS Imaging System Xenogen Bioluminescence Imaging System at different time points, and the fluorescence images and changes in fluorescence intensity at the tumor were recorded. After 24 hours, the

mice were sacrificed by cervical dislocation after anesthesia, and then the tumor, heart, liver, spleen, lung, and kidney were dissected out for small animal fluorescence imaging to evaluate the entry of nanoparticles into tumor tissue and organs.

MRI in vivo

BALB/c mouse model carrying 4T1 breast cancer was constructed. When the tumor volume reached 100mm^3, MRI scan in vivo imaging could be performed to explore the MRI imaging ability of ICG@SANPs-cRGD in the tumor. The tumor-bearing mice were injected with ICG@SANPs-cRGD and Gd-DTPA solution (100μL, 1mg/mL) through tail vein and scanned by 3.0T magnetic resonance instrument at different time points (0h, 1h, 2h, 3h, 4h, 5h, 6h) under anesthesia. TR: 825ms, TE: 11.5ms, matrix: 256 × 256mm; slice thickness 2.0mm, T1-weighted images of mice were obtained.

Clinical Observation of 4T1 Tumor Model

4T1 cells (1×10^6) were injected subcutaneously into the left side (primary tumor) of female BALB/c mice, and 6 days later, the tumor-bearing mice were randomly divided into 7 groups (n = 4): (1) PBS; (2) ICG@SANPs; (3) ICG@SANPs-cRGD; (4) NIR+ICG@SANPs; (5) NIR+ICG@SANPs-cRGD; (6) Anti-PD-L1; (7) NIR+ICG@SANPs-cRGD+Anti-PD-L1, then 4T1 cells were injected into the right side of the mice for the second tumor inoculation (distant metastases), ICG@SANPs and ICG@SANPs-cRGD were injected into mice at a dose of 5mg/kg, and NIR irradiation (808nm, 0.8W/cm^2, 3min) was performed every 12 hours after the injection in groups 4, 5, and 7. Anti-PD-L1 antibody (Clone: 10 F.9G2, Catalog No. BE0101, Bio XCell, USA) was administered intraperitoneally (i.p.) on days 1, 3 and 5 at a dose of 75 μg/mouse. During the experiment, the body weight, body temperature, and tumor volume of the mice were detected every other day, and photographs were taken. The tumor size was measured with a digital caliper, and the calculation method was as follows: tumor volume V (mm^3) = (width^2 × length)/2. According to the standard animal experiment protocol, when the tumor volume exceeded 1000mm^3, the mice were euthanized and the tumor and organ tissues were removed for detection.

Observation of Biosafety in vivo

After the experiment, the mice were sacrificed under anesthesia and the main organs were dissected out: heart, liver, spleen, lung, kidney, and blood were collected for testing, histological analysis with H&E staining, and various biochemical indices related to liver and kidney function and blood were determined by standard biochemical tests.

Detection of Relevant Indicators of Immune Activation in vivo

Blood samples were collected after treatment, and the inflammatory cytokines in serum were detected by ELISA Kit (Neobioscience, Guangzhou, China), including pro-inflammatory factors IL-6, IL-12, TNF-α, IFN-γ and anti-inflammatory factors TGF-β, IL-10 to assess acute inflammation induced by treatment. After the experiment, the mice were euthanized, the tumor was removed and sliced into 5μm sections. Histopathological analysis was performed with Hematoxylin-eosin stain kit (H&E) (Solarbio, Beijing, China). TdT-mediated dUTP nick-end labelling (TUNEL) (Beyotime Biotechnology, Shanghai, China) assay to analyze apoptosis in vivo. ROS production (Frozen section ROS detection kit (DHE probe) Baiaolaibo Technology Co., Ltd, Beijing, China), BAX protein (BAX Mouse Monoclonal Antibody, Beyotime Biotechnology, Shanghai, China), CD3 (CD3 epsilon Rabbit Monoclonal Antibody, Beyotime Biotechnology, Shanghai, China) and CD8 (CD8 alpha Rabbit Monoclonal Antibody, Beyotime Biotechnology, Shanghai, China) cytotoxic T lymphocytes, calretin CRT (Calreticulin Rabbit Monoclonal Antibody, Beyotime Biotechnology, Shanghai, China) and hypoxic inducible factor HIF-1 (HIF-1α antibody (mouse monoclonal antibody), Beyotime Biotechnology, Shanghai, China) were detected by immunofluorescence, Ki67 (Ki67 Rabbit Monoclonal Antibody, Beyotime Biotechnology, Shanghai, China) was detected by immunohistochemistry, and inflammatory factor secretion was detected by Elisa.

Statistical Analysis

Data were analyzed using descriptive statistics and analysis of variance and presented as mean values ± standard deviation. Comparisons between groups were performed by independent sample Student's *t*-test and analysis of variance. If $p > 0.05$, no statistical difference was considered. All analyses were repeated three times in three independent experiments ($*p < 0.05$, $**p < 0.01$, $***p < 0.001$ and $****p < 0.0001$).

Results and Discussion

Characterization of ICG@SANPs-cRGD

In the presence of surfactants, SANPs coated with oleic acid (OA) were synthesized by decomposition of metal acetyl acetone (ACAC) at high temperature, and SANPs were modified by PEG and cRGD molecules, as shown in Figure 1A. The synthesized ICG@SANPs and ICG@SANPs-cRGD have an ideal magnetic core-lipid-shell structure. TEM image (Figure 1B) showed that the synthesized ICG@SANPs-cRGD nanoparticles were clear in outline and dispersed in a spherical shape, with good consistency in particle size distribution. The particle size was 9.61 ± 1.434 nm, which was smaller than the critical size of Superparamagnetic 20–25nm of Fe_3O_4, showing superparamagnetic properties.[26]

Dynamic light scattering (DLS) measurements showed that the diameters of SANPs and ICG@SANPs were 19.74 ± 9.655 nm and 24 ± 16.473 nm, respectively. After loading cRGD, the diameter of ICG@SANPs-cRGD increased to 26.48 ± 16.127 nm (Figure 1C), indicating that cRGD was successfully loaded. In addition, we can also see from the figure that the size distribution range of magnetic nanoparticles is narrow. The peak value of hydration particle size of SANPs, ICG@SANPs and ICG@SANPs-cRGD nanoparticles is sharp with good dispersion, showing a relatively uniform size distribution range.

The zeta potential of SANPs was −46.63889 ± 9.687387 mv, and the negative zeta potentials of ICG@SANPs and ICG@SANPs-cRGD were −47.83091 ± 11.73301 mv and −25.16909 ± 11.73301 mv, respectively (Figure 1D), they stabilize the NPs in aqueous media through electrostatic repulsion, and the electrostatic interaction between SANPs and ICG@SANPs is responsible for the ICG loading. Compared with ICG@SANPs, the zeta potential of ICG@SANPs-cRGD was increased, indicating that cRGD molecules were successfully bound to ICG@SANPs.

In the ultraviolet-visible near-infrared absorption spectrum of ICG@SANPs-cRGD, the nanoparticles have a wide absorbance in the near-infrared region of 600–900nm, indicating that ICG@SANPs-cRGD prepared in this experiment

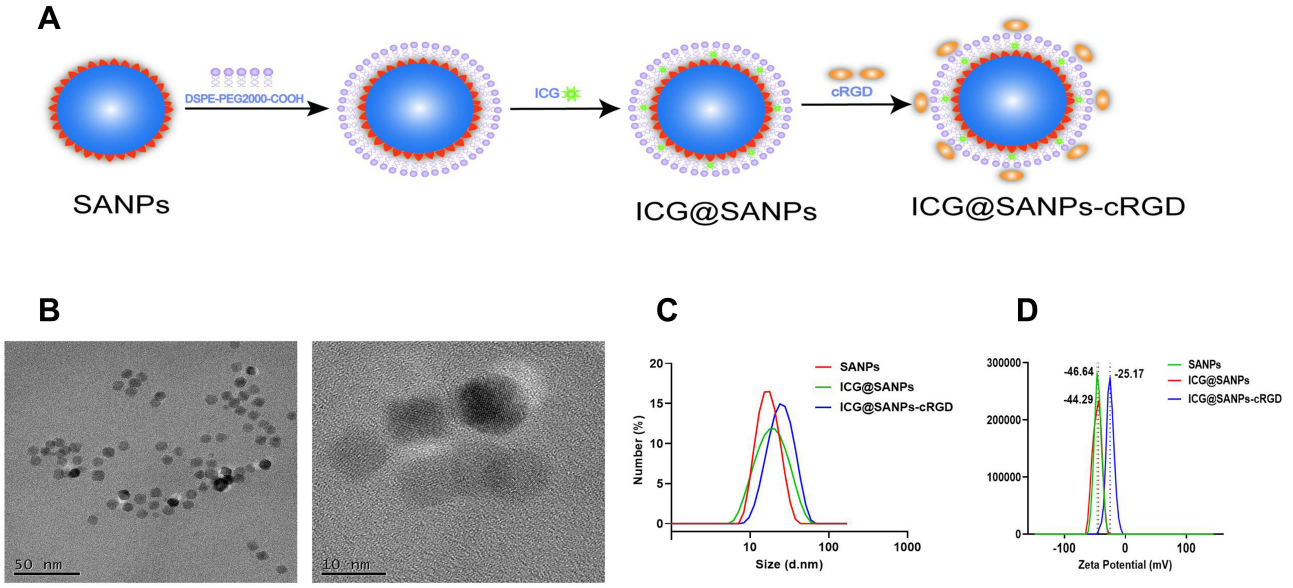

Figure 1 Synthesis and characterization of multifunctional nanoparticles. (**A**) Schematic illustration of the construction of ICG@SANPs-cRGD nanoparticles and their microstructures. (**B**) TEM image of ICG@SANPs-cRGD nanoparticles. (**C**) Size distributions of SANPs, ICG@SANPs, ICG@SANPs-cRGD nanoparticles. (**D**) Zeta potential of SANPs, ICG@SANPs, ICG@SANPs-cRGD nanoparticles.

has photothermal properties and has the potential to become a photothermal agent (Supplementary Figure 1). As shown in Supplementary Figure 2A, at room temperature (300K), the hysteresis loop of ICG@SANPs-cRGD shows a saturation magnetization value (Ms) of 0.017Oe, and the hysteresis loop has essentially no coercivity (Hc), exhibiting remarkable superparamagnetic properties. Generally speaking, the high Ms value of nanoparticles in the alternating current magnetic field (ACMF) will often obtain obvious magnetically induced heat generation and achieve enhanced MRI contrast effect,[27,28] which provides a basis for MRI imaging.

MRI Imaging Evaluation of ICG@SANPs-cRGD Nanoparticles in vitro

To explore the MRI imaging capability of ICG@SANPs-cRGD, we diluted it into nanosolutions with different concentrations. In the T1-weighted MRI images of ICG@SANPs-cRGD with different concentrations in Supplementary Figure 2B, it can be seen that with the increase of the concentration, under the direct action of the paramagnetic metal ion Fe_3O_4, the T1 shortens, the signal is enhanced, and the image brightness gradually increases, this may be due to the small size of ICG@SANPs-cRGD, the coupled magnetic moment of the Fe_3O_4 nanoparticles contained in it will decrease rapidly due to the decrease in size, which amplifies the effect of T1,[29] indicating that the ICG@SANPs-cRGD nanoparticles have MRI imaging capabilities.

Biosafety Assessment of ICG@SANPs-cRGD Nanoparticles

Nanomaterials must have good biocompatibility before they can be used in biomedical field, and hemolysis in blood is one of the evaluation indexes.[8] As shown in Supplementary Figure 3, when the concentration of ICG@SANPs-cRGD was less than 80 μg/mL, the hemolysis rate was lower than 10%, and even if the concentration of ICG@SANPs-cRGD increased to 100 μg/mL, the hemolysis rate did not increase significantly (<12%). The results showed that ICG@SANPs-cRGD showed a low hemolysis rate, which was also visually confirmed by the corresponding digital photos, which indicated that ICG@SANPs-cRGD had good biocompatibility and could be used in subsequent experiments.

Evaluation of the Cellular Internalization Ability of ICG@SANPs-cRGD Nanoparticles

Figure 2A shows the uptake of ICG@SANPs and ICG@SANPs-cRGD by 4T1 cells by confocal fluorescence imaging. The nucleoli of the two groups were uniformly blue stained, ICG@SANPs-cRGD co-cultured 4T1 cells exhibited strong red fluorescence in the cytoplasm, this means that ICG@SANPs-cRGD nanoparticles were taken up in large quantities by cells, while 4T1 cells treated with ICG@SANPs showed red fluorescence in the cytoplasm with weak fluorescence intensity. Supplementary Figure 4 also shows that the fluorescence intensity of ICG@SANPs-cRGD is stronger than that of ICG@SANPs ($p < 0.01$). This further indicates that the nanoparticles in this experiment can be taken up by cells, and the cRGD modification can improve the tumor targeting ability of the nanoparticles and ensure the killing effect.

Evaluation of Biocompatibility of ICG@SANPs-cRGD Nanoparticles in vitro

Nanoparticles used to specifically kill tumor cells generally have weak or no toxic or side effects on healthy cells in vivo.[30] In this paper, the toxicity of ICG@SANPs-cRGD nanoparticles on L929 and AML-12 healthy cell lines was first investigated. In Supplementary Figure 5, it was observed that ICG@SANPs-cRGD had little effect on the cell viability of L929 and AML-12 healthy cells in the range of 0–100 μg/mL, and the change of cell viability with the increase of concentration was not significant. These results indicate that ICG@SANPs-cRGD nanoparticles have no significant cytotoxicity to L929 and AML-12 healthy cell lines, and ICG@SANPs-cRGD has excellent biosafety, providing a safe basis for subsequent in vivo imaging and in vivo anti-tumor therapy.

Evaluation of PTT Capability of ICG@SANPs-cRGD Nanoparticles in vitro

Through the photothermal performance test of ICG@SANPs-cRGD, as shown in Figure 2B, after irradiation with 808nm laser, the temperature of 1×PBS solution increased only 2.8°C, while the temperature of ICG@SANPs-cRGD nanoparticle solution increased with the increase of concentration. Even the temperature of 5μg/mL nanoparticle solution also increased 13.5°C. As can be seen in Figure 2C, the temperature of ICG@SANPs-cRGD solution increased significantly with the increase of near-infrared power density. The results showed that ICG@SANPs-cRGD nanoparticles had

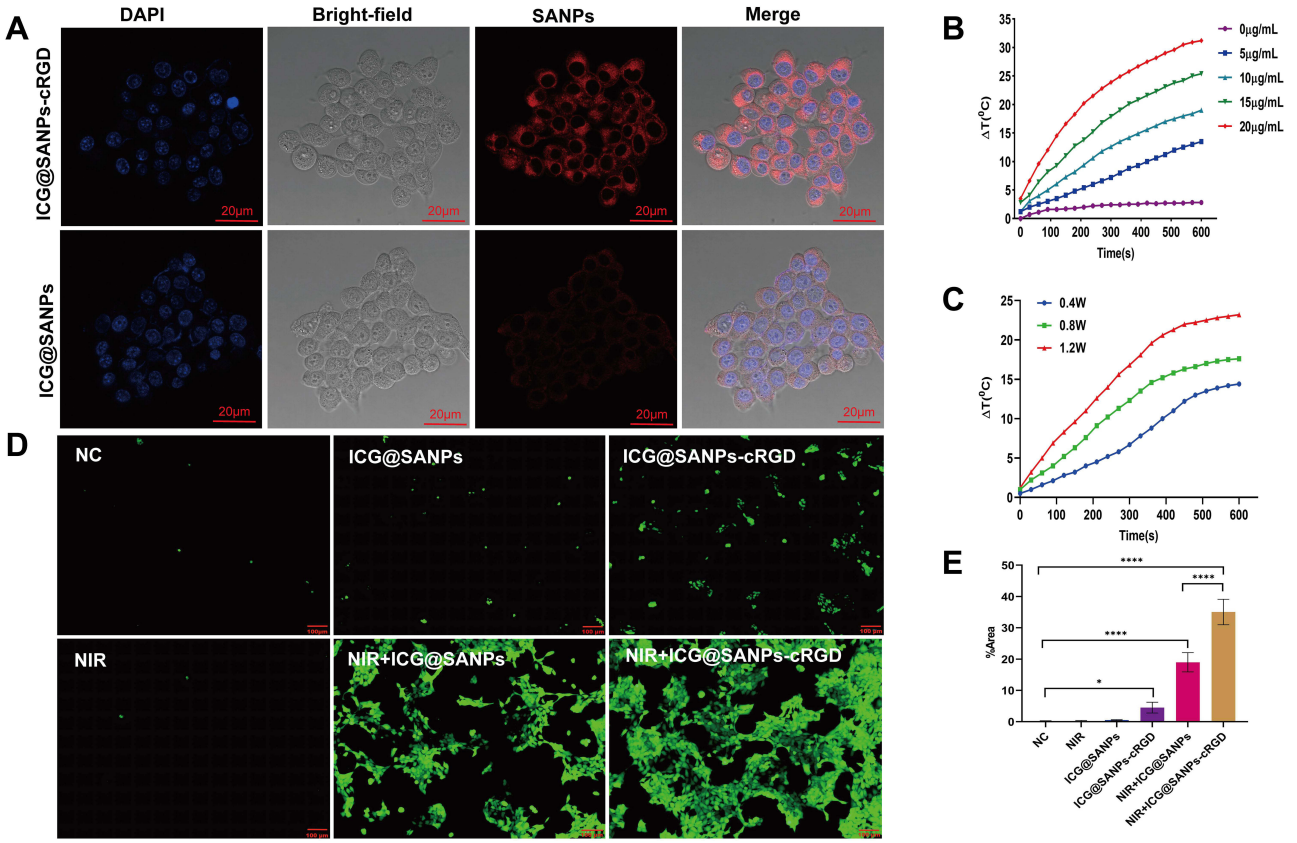

Figure 2 Cellular internalization of ICG@SANPs-cRGD nanoparticles and mechanism of PTT and PDT in vitro. (**A**) Cellular uptake of ICG@SANPs, ICG@SANPs-cRGD in 4T1 cells. (**B**) The temperature changes of five different concentrations of ICG@SANPs-cRGD nanoparticles under near-infrared light irradiation with power density of 0.8w/cm2 and wavelength of 808nm. (**C**) The temperature changes of the same concentrations of ICG@SANPs-cRGD(10μg/mL) under different power densities of NIR (0.4w, 0.8w and 1.2w) with a wavelength of 808nm. (**D**) Representative pictures of ROS production in 4T1 cells after different treatments (scale bar = 100μm). (**E**) Quantitative fluorescence area ratio of ROS generation in 4T1 cells after different treatments. (Data are expressed as means ± SD (n = 3). Statistical significances were calculated via ANOVA, *$p < 0.05$, ****$p < 0.0001$).

excellent photothermal conversion performance and potential as a synergist for PTT in vitro under different concentrations and irradiation conditions, which provided a theoretical basis for the enhancement of anti-tumor effect of PTT in vitro by ICG@SANPs-cRGD.

Evaluation of PDT Capability of ICG@SANPs-cRGD Nanoparticles in vitro

To reveal the potential mechanism of PTT/PDT killing of tumor cells in vitro by ICG@SANPs-cRGD nanoparticles, the production level of intracellular ROS was detected by DCFH-DA, which specifically targets and labels ROS.[31,32] After NIR irradiation, both ICG@SANPs and ICG@SANPs-cRGD produced ROS intracellularly, as evidenced by green fluorescence in 4T1 cancer cells (Figure 2D), and there were statistical differences between these two groups compared with the other groups ($p < 0.0001$). In addition, the fluorescence intensities of ICG@SANPs before and after irradiation were significantly different ($p < 0.0001$), indicating that the photosensitizer ICG promoted ROS generation under NIR irradiation. However, compared with the other groups, the ICG@SANPs-cRGD+NIR group had the strongest fluorescence intensity, proving that a large amount of ROS was generated, which was related to the strong targeting of cRGD and the strong intracellular photodynamic activity.[33] In contrast, the green fluorescence intensity of NC group, NIR group, ICG@SANPs group and ICG@SANPs-cRGD group was basically not observed or relatively weak (Figure 2E). Therefore, we can conclude that the enhanced PDT effect of ICG@SANPs-cRGD can produce a large number of cytotoxic ROS in cells and further lead to apoptosis and/or necrosis of cancer cells. Therefore, it can be speculated that ICG@SANPs-cRGD can perform photodynamic therapy on tumors under NIR irradiation, and ICG@SANPs-cRGD can

play an anti-tumor effect in vitro as a synergist of PDT, providing a theoretical basis for ICG@SANPs-cRGD to enhance the therapeutic.

Effects of ICG@SANPs-cRGD PPT/PDT on 4T1 Cell Proliferation in vitro

It can be found in the experiment of CCK8 detecting the effect of ICG@SANPs-cRGD-enhanced PPT/PDT effect on the proliferation of 4T1 cells, there was no significant difference in cell viability among the NC, NIR, ICG@SANPs, and ICG@SANPs-cRGD groups ($p > 0.05$). ICG@SANPs and ICG@SANPs-cRGD did not significantly inhibit the proliferation of 4T1 cells, and the cell viability of the four groups was all greater than 85%, indicating that ICG@SANPs and ICG@SANPs-cRGD had good biocompatibility. However, the difference in cell viability between NIR+ICG@SANPs and NIR+ICG@SANPs-cRGD and other groups was statistically significant ($p<0.0001$), and the cell viability in NIR+ICG@SANPs-cRGD group (30.044 ± 1.657) was lower than NIR+ICG@SANPs group (67.074 ± 0.405), the comparison between the two groups was also statistically significant ($p < 0.0001$) (Figure 3A). The stronger ability of NIR+ICG@SANPs and NIR+ICG@SANPs-cRGD to inhibit cancer cells is because PTT converts light energy into heat energy through photothermal agent under NIR irradiation, and thermally ablated 4T1 cells; meanwhile, PDT relies on the photosensitizer ICG to convert light into cytotoxic reactive oxygen species and induce cell death, fully demonstrating the advantages of PTT/PDT synergistic therapy for cancer.[5] The cytotoxicity of NIR+ICG@SANPs-cRGD was stronger than that of NIR+ICG@SANPs group, which may be due to the better affinity, receptor selectivity and enzyme stability of cRGD.[34] In addition, ICG@SANPs-cRGD has stronger cellular internalization under NIR irradiation, and the photothermal conversion efficiency is higher under the high temperature action of PTT, resulting in more singlet oxygen, which makes up for the limitation of hypoxia in the process of PDT and improves the effect of PDT therapy. When studying the effect of ICG@SANPs-cRGDd concentration on PDT/PPT, we found that the survival rate of 4T1 cells decreased significantly with the increase of ICG@SANPs-cRGD nanoparticle concentration at 0.8W/cm^2 for 3min ($p < 0.0001$). There was no significant difference in cell viability between 10μg/mL and 15μg/mL groups ($P = 0.14$). The difference between the other groups was statistically significant ($p < 0.0001$) (Figure 3B). These results imply that ICG@SANPs-cRGD nanoparticles have a good in vitro PTT/PDT effect within a safe concentration range, and 10μg/mL can be used as a safe concentration for subsequent experiments.

In addition, we also analyzed the relationship between the effect of ICG@SANPs-cRGD mediated PDT/PPT with the same concentration (10μg/mL) and incubation time. The experiment found that the increase of incubation time reduced the viability of 4T1 cells ($p < 0.0001$) (Figure 3C). When co-incubated for 2h and 4h, there was no significant difference in the viability of 4T1 cells ($p = 0.205$). The results showed that the increase of incubation time reduced the viability of 4T1 cells, indicating that the PTT/PDT effect of ICG@SANPs-cRGD nanoparticles in vitro was time dependent.

Effects of ICG@SANPs-cRGD Enhanced PTT/PDT on 4T1 Cell Clonal Formation

In the clone formation experiment, the number of cell clones in the NC, NIR, ICG@SANPs, and ICG@SANPs-cRGD groups was similar, and the difference was not statistically significant ($p > 0.05$); In addition, compared with the first four groups, the number of cloned cells in the NIR+ICG@SANPs and NIR+ICG@SANPs-cRGD groups decreased ($p<0.01$); It is worth noting that the number of cells in the NIR+ICG@SANPs-cRGD group was significantly less than that in the other groups ($p<0.01$) (Figure 3D, Supplementary Figure 6), this result was consistent with the above results that ICG@SANPs-cRGD inhibited the proliferation of 4T1 cells in vitro by PPT/PDT, which again confirmed that ICG@SANPs-cRGD enhanced the powerful inhibitory effect of PTT/PDT on the proliferation of tumor cells. This result was consistent with the above results that ICG@SANPs-cRGD inhibited the proliferation of 4T1 cells in vitro by PPT/PDT, which again confirmed that ICG@SANPs-cRGD enhanced the powerful inhibitory effect of PTT/PDT on the proliferation of tumor cells.

Effects of ICG@SANPs-cRGD-Enhanced PTT/PDT on Cell Death State

In order to further verify that PTT/PDT based on ICG@SANPs-cRGD has a high ability to kill 4T1 tumor cells, Calcein-AM/PI double staining method was used to compare the survival status of 4T1 cells under different treatments. As shown in Figure 3E and Supplementary Figure 18, few cells in NC, NIR, ICG@SANPs and ICG@SANPs-cRGD groups

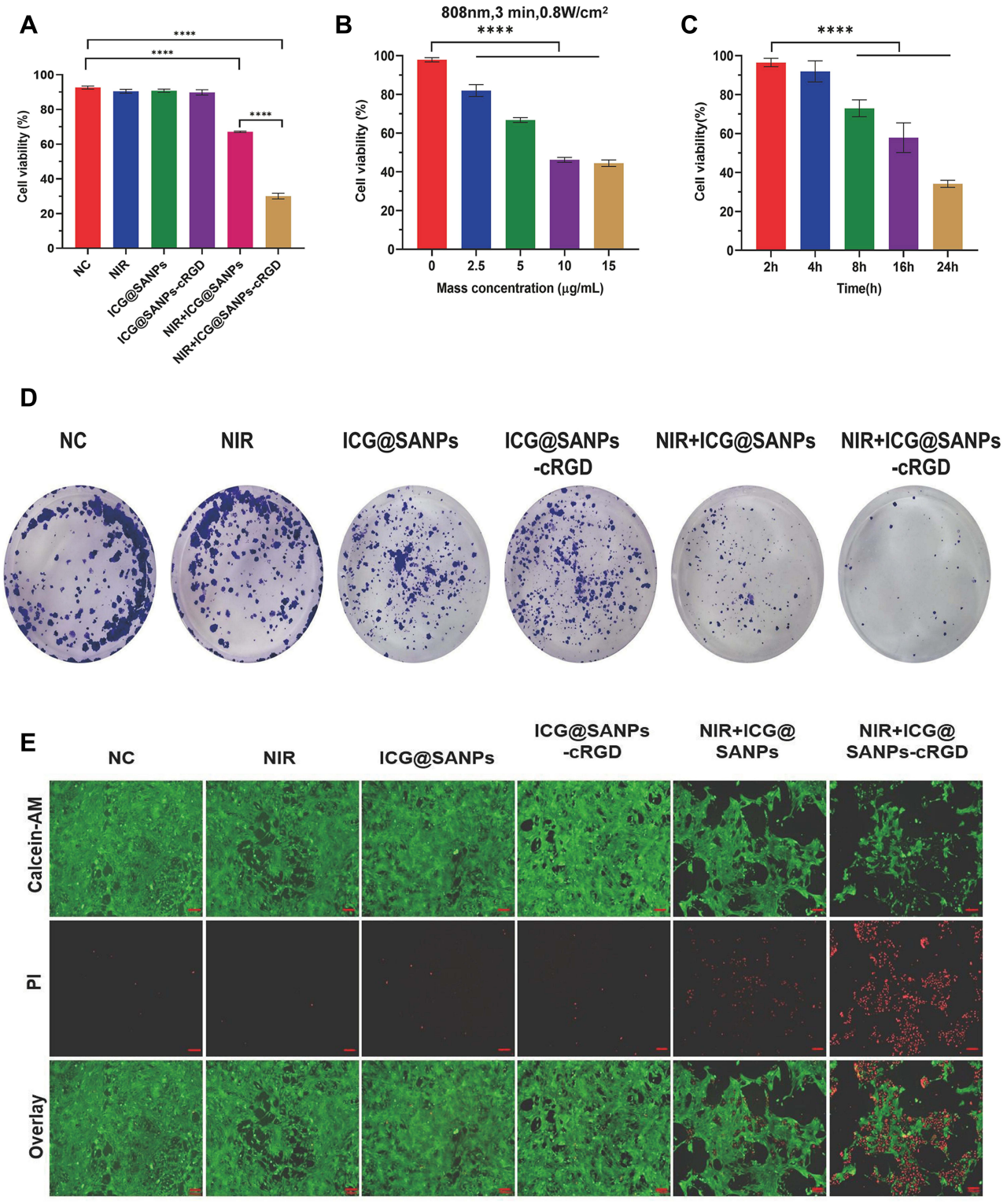

Figure 3 Effects of ICG@SANPs-cRGD mediated PTT/PDT on 4T1 cell proliferation and survival in vitro. (**A**) Cell viability of 4T1 cells under different treatment methods. (**B**)The effect of the concentration of ICG@SANPs-cRGD on the effect of PTT/PDT in vitro. (**C**) The effect of incubation time on the effect of PTT/PDT in vitro. (**D**) Representative pictures showing the colonies formed of 4T1 cells after different treatment. (**E**) Fluorescence microscopy images of 4T1 cells stained with calcein AM/PI under different treatments (scale bar = 100μm). (Data are expressed as means ± SD (n = 3). Statistical significances were calculated via ANOVA, ****$p < 0.0001$).

showed red fluorescence (dead cells), while most cells showed green fluorescence (living cells). Under the same conditions, when irradiated with 808 nm near-infrared laser, some cells in the NIR+ICG@SANPs group showed red fluorescence, and some dead cells showed red fluorescence. However, a large number of 4T1 cells in the NIR +ICG@SANPs-cRGD group showed red fluorescence, indicating a large number of cell death. Compared with other groups, the NIR+ICG@SANPs-cRGD group had a higher ability to kill tumor cells. The staining results of the Calcein-AM/PI double staining method were consistent with the above cytotoxicity experiments and other cell function experiments, which once again proved that NIR+ICG@SANPs-cRGD enhanced the ability of PTT/PDT to kill tumor cells.

Study on Near-Infrared Photothermal Effect of ICG@SANPs-cRGD in vivo

In order to prove that ICG@SANPs-cRGD also has photothermal effect in vivo and can be used for photothermal therapy and combined therapy of tumors, we performed in vivo near-infrared photothermal studies using an infrared thermal imager. After modeling, the tumor-bearing mice were randomly divided into three groups: 1×PBS, ICG@SANPs, and ICG@SANPs-cRGD for observation. In Figure 4A, temperature changes of tumor sites under 808nm near-infrared irradiation can be intuitively detected. The temperature of tumor sites of mice treated with ICG@SANPs and ICG@SANPs-cRGD showed an obvious trend of increase with the increase of irradiation time. However, the temperature increase of tumor site in 1×PBS group was relatively small. As can be seen from Figure 4B, the temperature of ICG@SANPs-cRGD continued to increase within 3 min under the irradiation of near-infrared light, with a maximum increase of about 15°C. The temperature of tumor area of mice treated with ICG@SANPs increased by about 8°C after NRI irradiation for 3min. However, the temperature of the 1×PBS group basically did not change significantly. However, for the tumor site temperature of the mice injected with ICG@SANPs-cRGD, there was a significant increase trend with the increase of irradiation time, which was statistically significant compared with the other two groups (p<0.0001). Although the temperature of the tumor site of the mice in the ICG@SANPs group increased, it was significantly lower

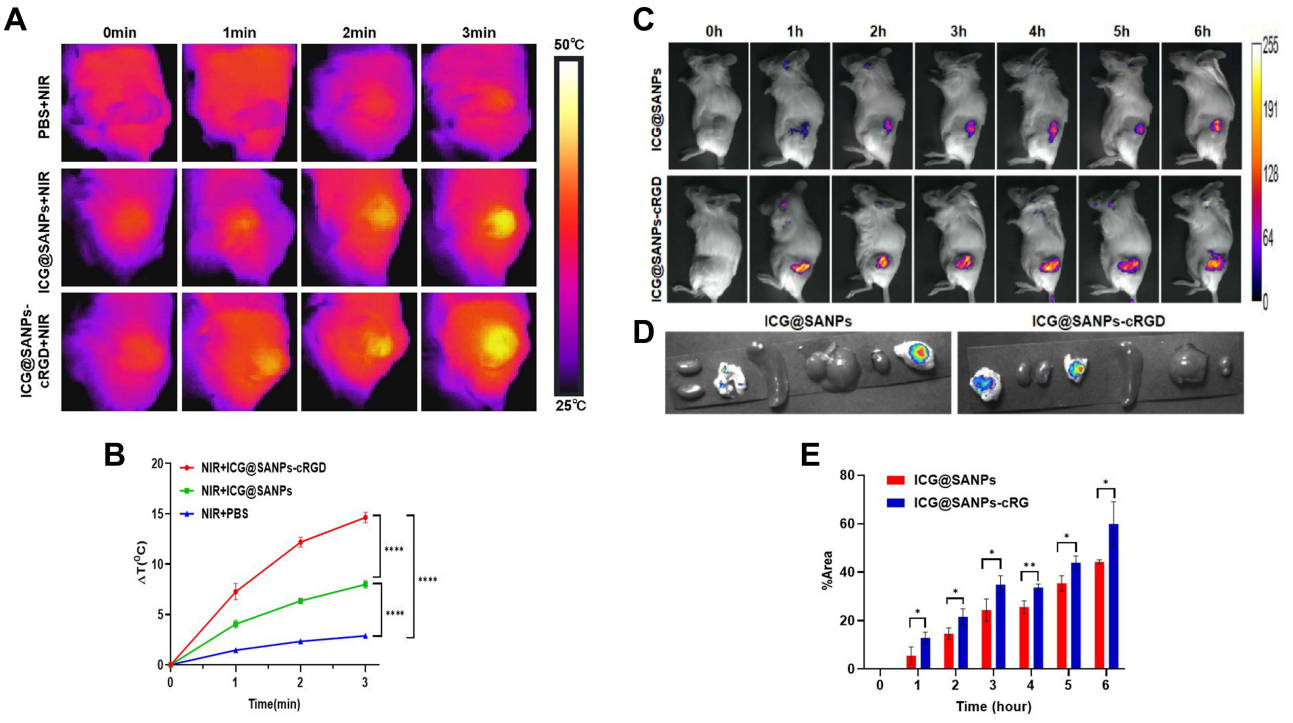

Figure 4 In vivo photothermal effect and fluorescence imaging ability of ICG@SANPs-cRGD. (**A**) In vivo photothermal effect of ICG@SANPs, 1×PBS, ICG@SANPs-cRGD with 808nm laser irradiation. (**B**) The temperature curve of 4T1 tumour-bearing mice exposed to 808nm laser within 3min (Data are expressed as means ± SD (n = 3). Statistical significances were calculated via ANOVA, ****p < 0.0001). (**C**) Fluorescence imaging of in vivo tumor tissue at different time points after tail vein injection of nanoparticles and (**D**) fluorescence imaging of isolated organs. (**E**) Fluorescence area ratio of tumor tissues at different time (Data are expressed as means ± SD (n = 3). Statistical significances were calculated via Student's t test, *p < 0.05, **p < 0.01).

than that in the ICG@SANPs-cRGD group ($p<0.0001$). The temperature increase in the tumor site of the mice in the 1×PBS group was negligible compared with the other two groups and was statistically significant compared with the other two groups ($p< 0.0001$). This result shows that the temperature generated by laser irradiation itself is relatively low, which is not enough to thermally ablate the tumor, and the changes brought by the temperature will not cause damage to the skin and surrounding organs of mice, while ICG@SANPs-cRGD nanoparticles can effectively convert light energy into heat energy under the irradiation of near-infrared light, which promotes the rapid increase of the temperature of the tumor site. These results provide guidance for phototherapy and prove that ICG@SANPs-cRGD can accumulate in large quantities in tumor and is stable in nature, showing high photothermal conversion ability. The surface temperature of tumor is up to 53.1°C, which proves that photothermal therapy with ICG@SANPs-cRGD is completely feasible.

In vivo Fluorescence Imaging Analysis of ICG@SANPs-cRGD

In order to detect the distribution and near-infrared fluorescence imaging ability of ICG@SANPs-cRGD nanoparticles in vivo, through tail vein injection of ICG@SANPs and ICG@SANPs-cRGD, the dynamic fluorescence changes and accumulation at the tumor site were monitored in real time with the help of a fluorescence imaging system. As shown in Figure 4C, the strong fluorescence signal of ICG@SANPs-cRGD was found at the tumor site 1h after injection, and the fluorescence intensity gradually increased even 6 hours after injection, ICG@SANPs showed strong fluorescence signal only 4h after injection, and the signal intensity was still weaker than ICG@SANPs-cRGD. This indicates that ICG@SANPs-cRGD can be rapidly targeted and enriched to tumor tissues through enhanced permeability and retention effect (EPR) of solid tumors, accumulate at tumor sites, and continue to play a role. This is related to the small size of ICG@SANPs-cRGD nanoparticles that can be easily targeted into the tumor site and the lack of lymphatic system at the tumor site.[35] Figure 4D shows the ex vivo fluorescence signals of dissected tumor tissues and organs 24h after ICG@SANPs-cRGD injection. Fluorescence signal results of in vitro tissues showed that tumor tissues had strong fluorescence signal, and there was a small amount of fluorescence signal in lungs, while no fluorescence signal in other organs, indicating that ICG@SANPs-cRGD nanoparticles were highly targeted and mainly concentrated in tumor sites. Almost no aggregation in other organs also indicates that the nanoparticles have relatively high bioavailability and almost no potential systemic toxicity, thus they can play their photothermal and photodynamic anti-tumor effects safely and effectively. Quantitative analysis of the fluorescence signal at the tumor site is shown in Figure 4E. The fluorescence intensity of the two groups of mice treated with ICG@SANPs and ICG@SANPs-cRGD nanoparticles increases with time. However, at each time point, the fluorescence intensity of tumor sites in the mice treated with ICG@SANPs-cRGD nanoparticles was higher than that in the ICG@SANPs group, and the difference was statistically significant ($p<0.05$). Once again, ICG@SANPs-cRGD nanoparticles demonstrated good tumor targeting in vivo, stability of EPR effect, and longer blood circulation time.

MRI Imaging Analysis of ICG@SANPs-cRGD in vivo

Gd-DTPA (Gadolinium-Diethylenetriaminepentaacetic Acid) and ICG@SANPs-cRGD were injected into the tail vein of mice to examine their MRI imaging ability in vivo, 3.0T MRI scans were performed before injection (0h) and after injection (2h-6h). MRI images (Supplementary Figure 7) showed shortening of T1, enhancement of signal, and increase of image brightness with increasing cycle time. It can be seen that the signal enhancement in the tumor site of mice injected with Gd-DTPA in the first two hours is faster than that of ICG@SANPs-cRGD. The T1 signal at the tumor site increased slowly at the 3rd hour, while the signal increase at the tumor site injected with ICG@SANPs-cRGD showed a steady upward trend, showing a better ability of MRI imaging contrast. This may be due to the short circulation time of Gd-DTPA as a T1-weighted MRI contrast agent, which cannot achieve specific imaging at the tumor site, cRGD modified ICG@SANPs-cRGD has specific targeting and ERP effect at tumor site as well as good longitudinal relaxation rate.[36] These results indicate that ICG@SANPs-cRGD nanoparticles have higher tumor targeting ability, can effectively target tumor tissues, aggregate at tumor sites, and can perform specific T1-weighted MRI detection for breast cancer. It is also indicated that ICG@SANPs-cRGD nanoparticles have great potential to guide PDT/PTT therapy in vivo magnetic resonance imaging and provide experimental basis for the integration of tumor diagnosis and treatment.

Evaluation of Anti-Tumor Effect of PDT/PTT Combined Immunotherapy Based on ICG@SANPs-cRGD in vivo

At present, the requirement of cancer treatment is not only to destroy the primary tumor but also to identify, inhibit and eliminate the distant metastasis of the tumor. Anti-PD-L1 has been shown to promote anti-tumor immunity by inhibiting the exhaustion of cytotoxic T lymphocytes and achieve good clinical therapeutic effect, especially when it is combined with other treatment regimens, the anti-tumor effect is significantly enhanced.[37] Therefore, on the basis of in vitro experimental results, this study further explored the anti-tumor effect of ICG@SANPs-cRGD-based PTT/PDT therapy in vivo by using combined Anti-PD-L1 immunotherapy.

To evaluate the in vivo antitumor efficacy of ICG@SANPs-cRGD-based PDT/PTT combined with Anti-PD-L1 immunotherapy, a bilateral subcutaneous 4T1 tumor model was used. The experimental procedure is shown in Figure 5A, the tumor on the left was designated as the primary tumor, and the tumor on the right was considered as a distant metastasis. Figure 5C and D show the treatment results of different groups for primary and simulated distant metastatic tumors. The figure shows the inhibitory effect of PBS, ICG@SANPs, ICG@SANPs-cRGD, NIR +ICG@SANPs, NIR+ICG@SANPs-cRGD, Anti-PD-L1 on primary and distant metastatic tumors were significantly weaker than the NIR+ICG@SANPs-cRGD+Anti-PD-L1 group. Although ICG@SANPs-cRGD mediated PTT/PDT therapy alone inhibited primary tumor growth, it did not inhibit distant tumors. Anti- PD-L1 alone has a certain inhibitory effect on distant tumors, but it does not play a good effect in primary tumors, indicating that ICG@SANPs-cRGD enhances the therapeutic effect of PDT/PTT combined immune checkpoint agent on primary tumors and distant metastatic tumors. The combination of PDT/PTT and immunotherapy was superior to single therapy in inhibiting the primary tumor and distant metastatic tumor. Notably, the PDT/PTT combined with Anti-PD-L1 treatment based on ICG@SANPs-cRGD not only exhibited strong inhibitory effects in primary 4T1 tumors but also significantly inhibited the growth of distant tumors (Figure 5B, Supplementary Figure 8), these results suggest that Tumor-specific immune

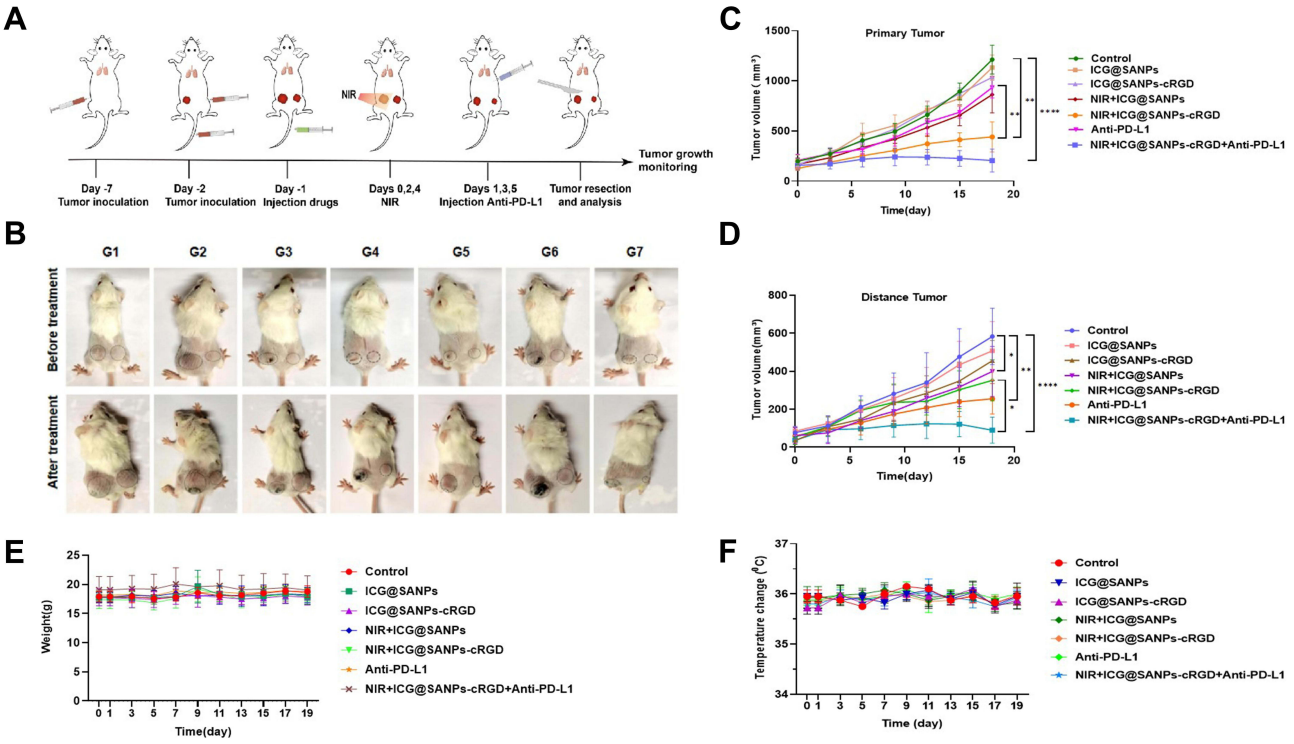

Figure 5 Combined therapy-mediated antitumor effect in the 4T1 tumor model. (**A**) Establishment and treatment of 4T1 tumor model; (**B**) Tumor photos of 4T1 tumor-bearing mice before and after treatment; (**C** and **D**) primary (**C**) and distant (**D**) tumour-growth curves of different groups of tumour-bearing mice after various treatments as indicated in the figure. Error bars are based on SD (n = 4); E, F time-dependent body weight (**E**) and temperature (**F**) surveillance of mice (n = 4) after different treatments. G1: Control; G2: ICG@SANPs; G3: ICG@SANPs-cRGD; G4: NIR+ICG@SANPs; G5: NIR+ICG@SANPs-cRGD; G6: Anti-PD-L1; G7: NIR+ICG@SANPs-cRGD+Anti-PD-L1 (Data are expressed as means ± SD (n = 4). Statistical significances were calculated ANOVA, *$p < 0.05$, **$p < 0.01$ and ****$p < 0.0001$).

responses mediated by PDT/PTT therapy based on ICG@SANPs-cRGD sensitize tumors to Anti-PD-L1 immunotherapy and enhance the effect of immunotherapy. PDT/PTT combined with Anti-PD-L1 therapy may be an effective treatment strategy for cancer patients.

In addition, there were no abnormal changes in body weight and body temperature of mice in the NIR+ICG@SANPs-cRGD+Anti-PD-L1 group (Figure 5E and F), and there was no abnormal effect on the behavior of the mice. These results again indicated that PDT/PTT combined with Anti-PD-L1 immunotherapy strategy had a relatively high biosafety and showed no significant systemic toxicity.

Biosafety Evaluation of PDT/PTT Combined Immunotherapy Based on ICG@SANPs-cRGD in vivo

To demonstrate the biosafety of ICG@SANPs-cRGD-enhanced PTT/PDT combined with Anti-PD-L1 therapy, the potential harm to normal organs of this combined treatment modality was evaluated. H&E staining was performed on the main organs (heart, liver, spleen, lung and kidney) of 4T1 tumor-bearing mice after different treatments, and the results showed no obvious inflammation and histological damage in the main organs, supporting the non-toxicity and biosafety of ICG@SANPs-cRGD nanoparticles (Supplementary Figure 9). In addition, healthy mice were used as healthy control group. Blood routine and biochemical tests of liver and kidney functions were performed on tumor-bearing mice treated with NIR+ICG@SANPs-cRGD+Anti-PD-L1. The results showed that there were no significant differences in all measurement indexes between the treatment group and the healthy control group (Supplementary Figure 10), which also confirmed that the PDT/PTT combined with Anti-PD-L1 treatment based on ICG@SANPs-cRGD had no significant toxicity and had good histocompatibility. In conclusion, our results suggest that PDT/PTT combined with Anti-PD-L1 therapeutic strategy based on ICG@SANPs-cRGD has good biocompatibility and can be used in subsequent experiments, with great potential in cancer therapy.

Study on the Immune Activation Mechanism of PDT/PTT Combined Immunotherapy Based on ICG@SANPs-cRGD

The breast cancer 4T1 mouse tumor model demonstrates that ICG@SANPs-cRGD nanoparticles can enhance the therapeutic effect of PDT/PTT combined with Anti-PD-L1 therapy in mouse solid tumors. The following is a preliminary exploration of the immune effect activation mechanism of ICG@SANPs-cRGD nanoparticles in enhancing the in vivo therapeutic effect of PDT/PTT combined with Anti-PD-L1. We observe the effect of ICG@SANPs-cRGD mediated combination therapy on immune-related indexes and immune activation effect.

The ability of PDT/PTT combined with Anti-PD-L1 treatment based on ICG@SANPs-cRGD to induce local cancer cell apoptosis or necrosis in vivo under NIR irradiation was explored by H&E staining experiments. As shown in Figure 6A, most tumor cells in tumor tissues of mice treated with 1×PBS, ICG@SANPs, ICG@SANPs-cRGD, NIR+ICG@SANPs and Anti-PD-L1 were relatively dense and basically complete in structure. In contrast, the tumor treated with NIR+ICG@SANPs-cRGD and NIR+ICG@SANPs-cRGD+Anti-PD-L1 showed significantly isolated and sparse tumor cells. Cells in NIR-irradiated ICG@SANPs-cRGD+Anti-PD-L1 treated tumor tissue showed extensive nuclear shrinkage. This result was also verified by the high percentage of TUNEL positive cells (red fluorescence) in TUNEL analysis (Figure 6B, Supplementary Figure 11). These results suggest that ICG@SANPs-cRGD enhances the effect of PDT/PTT combined immunotherapy, while NIR irradiation ICG@SANPs-cRGD enhances the large number of ROS produced by PDT action, activates adaptive and innate anti-tumor immunity, and promotes tumor immunogenic cell death.[38] ICG@SANPs-cRGD enhanced PTT can stimulate the host immune system and enhance the immune activity of the body by releasing tumor antigens from apoptotic and necrotic tumor cells into the tumor microenvironment and promoting the release of tumor-derived antigens into T cells.[39,40] In addition, it also enhanced the effect of Anti-PD-L1 immunotherapy, causing severe damage to tumor tissue, resulting in more apoptosis and necrosis of tumor cells, and at the same time increasing the gap between tumor tissues, which is beneficial to ICG@SANPs-cRGD penetrates deeper into the tumor more easily and plays a better role in eliminating 4T1 solid tumors. In addition, BAX, as a water-soluble related protein homologous to BCL-2, is a pro-apoptotic gene in the BCL-2 gene family. Overexpression of BAX can antagonize the protective effect of BCL-2 and make cells tend to die.[41] The expression changes of BAX were detected by tissue

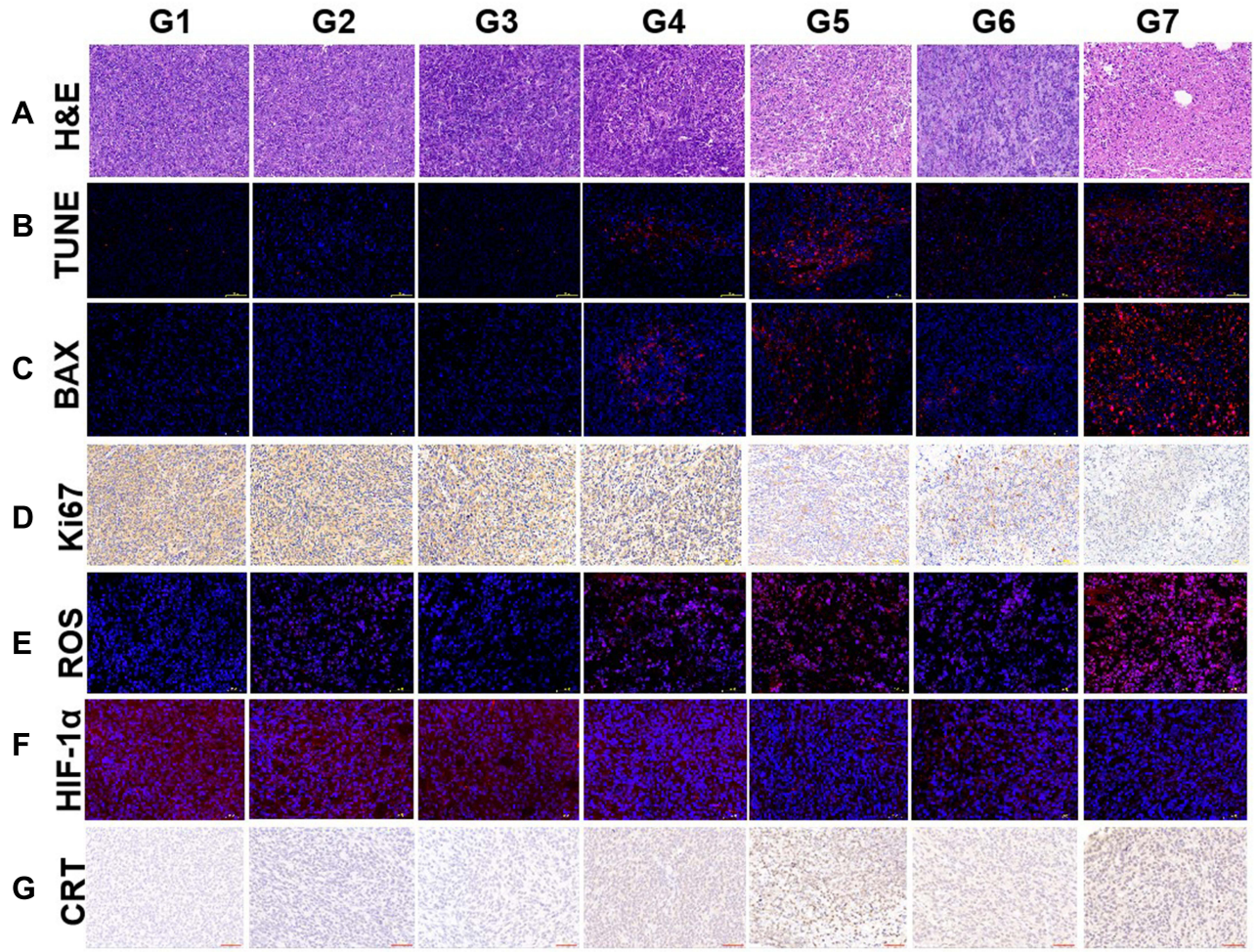

Figure 6 Effects of PDT/PTT combined with Anti-PD-L1 immunotherapy based on ICG@SANPs-cRGD on 4T1 cell apoptosis and immune related indexes in tumor tissues (scale bar = 50μm). (**A**) H&E staining of cells in tumor tissue after treatment. (**B**) TUNEL staining of tumor tissue after treatment. (**C**) Bax protein expression in tumor tissue after treatment. (**D**) Expression of Ki67 under different treatments. (**E**) ROS produced in tumor tissue under different treatments. (**F**) Changes of HIF-1α expression under different treatments. (**G**) Expression changes of CRT under different treatments. G1: Control; G2: ICG@SANPs; G3: ICG@SANPs-cRGD; G4: NIR+ICG@SANPs; G5: NIR+ICG@SANPs-cRGD; G6: Anti-PD-L1; G7: NIR+ICG@SANPs-cRGD+Anti-PD-L1.

immunofluorescence assay to further explain one of the immune mechanisms of the combination therapy with strong anti-solid tumor ability. As can be seen from Figure 6C, the fluorescence intensity of BAX gene (red fluorescence) in NIR+ICG@SANPs-cRGD+Anti-PD-L1 group was the strongest, indicating that a large number of cells in the tumor tissues had undergone apoptosis, which was also proved in Supplementary Figure 12. These results suggest that PDT/PTT combined with Anti-PD-L1 immunotherapy based on NIR+ICG@SANPs-cRGD activated and promoted the high expression of BAX gene, which antagonized the protective effect of BCL-2 and led to the death of 4T1 tumor cells. In addition, the activated BAX gene plays a key role in cell survival by mediating the programmed cell death process.[42,43] Changes in the expression of BAX gene caused changes inside and outside the mitochondrial membrane, and then cytochrome C was released into the cytoplasm, which activated the mitochondrial apoptosis pathway and also led to the apoptosis of 4T1 cells.[44] Therefore, the increased expression of BAX gene after combination therapy plays an important role in enhancing immune function and fighting breast cancer.

Ki-67 antigen is a protein related to nuclear division and proliferation. The expression of Ki-67 is closely related to the proliferation and growth of tumor cells and is often used as a reliable marker of tumor cell proliferation activity, which is essential in tumor cell proliferation.[45] Therefore, immunohistochemical staining was used to detect the expression of tumor proliferation antigen Ki-67 at the tissue level in this study to explore the mechanism of PDT/PTT combined with Anti-PD-L1 immunotherapy based on multifunctional ICG@SANPs-cRGD nanoparticles. The results of Ki67 staining in Figure 6D showed that the NIR +ICG@SANPs-cRGD+Anti-PD-L1 group significantly inhibited the proliferation of 4T1 cells in the tumor tissue, which

eventually led to the regression of the tumor tissue, showing the best tumor inhibitory effect. Quantitative analysis results of Supplementary Figure 13 showed that among all experimental groups, Ki67 expression level in tumor tissues of NIR +ICG@SANPs-cRGD+Anti-PD-L1 group was the lowest ($p < 0.0001$). The above results show that the ROS generated by ICG@SANPs-cRGD-mediated PDT/PTT combined with Anti-PD-L1 treatment under NIR irradiation can directly oxidize lipids, proteins and DNA in cells and inhibit the production of tumor proliferation antigen Ki67. It inhibits the division of tumor cells, thereby achieving the purpose of inhibiting the proliferation of 4T1 tumor cells, showing a good anti-tumor effect in vivo.[46,47] The generation and accumulation of intracellular ROS is an important inducer of cytotoxicity in PDT therapy, and ROS can affect the tumor immune response by regulating the phenotype and function of tumor cells and immune cells.[48] As can be seen in Figure 6E, ROS (red fluorescence) was generated in tumor tissues of ICG@SANPs, ICG@SANPs-cRGD and ICG@SANPs-cRGD+Anti-PD-L1 groups under NIR irradiation. The ROS amount produced by ICG@SANPs-cRGD+ Anti-PD-L1 irradiation was the largest. In Supplementary Figure 14, it can also be seen that the three groups under NIR irradiation produced the most ROS, and these three groups were statistically significant compared with the other groups ($p<0.0001$). These results indicated that ICG@SANPs-cRGD nanoparticles enhanced the anti-tumor effect of PDT under NIR irradiation, produced a large number of cytotoxic ROS, induced immunogenic death of tumor cells, activated the immune response, enhanced the effect of immune checkpoint blocker Anti-PD-L1, and led to apoptosis of tumor cells. Therefore, the combination therapy based on ICG@SANPs-cRGD mediates the immune response by increasing ROS production and enhances the therapeutic effect of tumors.

During the rapid growth of 4T1 tumors, it often leads to tumor ischemia and hypoxia, hypoxia stress in tumor microenvironment can induce significantly increased transcription activity of HIF-1, promote the formation of new blood vessels of tumor cells under hypoxia condition, and enhance the ability of tumor invasion and migration, at the same time, it will accelerate the metastasis of tumor cells to other organs along with blood circulation, resulting in poor prognosis of tumor.[49] Activation of HIF-1α is closely associated with a variety of tumor and carcinogenic pathways, so blocking HIF-1α itself or proteins interacting with HIF-1α can inhibit tumor growth.[50] In addition, studies have shown that under hypoxic conditions, PD-L1 in cancer cells also increases with the increase of HIF-1α, which leads to the apoptosis of cytotoxic T cells and the immune escape of tumor cells.[51] Therefore, in this study, the effect of PDT/PTT combined with anti-PD-L1 treatment on HIF-1α expression. As shown in Figure 6F, NIR+ICG@SANPs-cRGD+Anti-PD-L1 group represented the weakest red immunofluorescence, indicating that HIF-1α expression was the least, and blood vessels were the most abundant. Level based on ICG@SANPs-cRGD was studied to explore the mechanism of anti-tumor immune response of combined therapy. It can also be seen in Supplementary Figure 15 that the expression of HIF-1α was the lowest in the NIR+ICG@SANPs-cRGD+Anti-PD-L1 group. These results indicate that ICG@SANPs-cRGD has superior photothermal conversion ability under NIR irradiation, which enhances the effect of PTT, leads to tumor site temperature rise, tumor vascular dilation, improves the hypoxic tumor microenvironment, alleviates tumor ischemia and hypoxia, and overcomes the inhibition of tumor hypoxic environment on PDT therapeutic effect, decreased the expression level of HIF-1α and activated the immune response. Anti-PD-L1 blocks the binding of PD-L1 ligands in cancer cells to PD-1 protein on T cells, activates the immune activity of T cells, and prevents the immune escape of tumor cells.[52] Therefore, PDT/PTT combined with Anti-PD-L1 therapy based on ICG@SANPs-cRGD under NIR irradiation inhibited the activity of HIF-1α, greatly improved the hypoxic microenvironment of the tumor site, and showed a good tumor therapeutic effect.

In situ tumor-activated immunogenic cell death effects combined with immune checkpoint blockade therapy are sufficient to induce systemic immune effects. Immunogenic cell death is a specific variant of regulatory cell death, driven by stressors such as ROS.[53] Calreticulin (CRT) acts as a marker of cellular immunogenic death, and its protein is everted to the cell membrane surface under the stimulation of combination therapy, transmits a "eat me" signal to immune cells; meanwhile, CRT also stimulates macrophages and dendritic cells to engulf dying cells and their apoptotic debris, further induces T cell enrichment, and enhances the immunogenic recognition and phagocytosis of dead tumor cells by antigen-presenting cells.[54] As shown in Figure 6G, CRT signals were the most in tumors treated by NIR+ICG@SANPs-cRGD +Anti-PD-L1 group. It can also be seen in Supplementary Figure 16 that among all the treatment groups, the expression of CRT was the highest in the NIR+ICG@SANPs-cRGD+Anti-PD-L1 group ($p<0.0001$). These results indicated that PDT/PTT combined with anti-PD-L1 treatment based on ICG@SANPs-cRGD significantly induced CRT exposure, enhanced the role of antigen presenting cells, promoted cell immunogenic death, induced systemic immune response, and enhanced the effect of tumor immunotherapy.

Many studies have demonstrated that a high proportion of $CD3^+$ and $CD8^+$ cytotoxic T lymphocyte infiltration in tumors can be used as biomarkers to evaluate good prognosis and clinical efficacy.[55,56] As shown in Figure 7A and Supplementary Figure 17, PDT/PTT combined with Anti-PD-L1 treatment based on ICG@SANPs-cRGD stimulated the most infiltration of $CD3^+$T cells and $CD8^+$T cells in distant tumor tissues. No or minimal tumor infiltration of

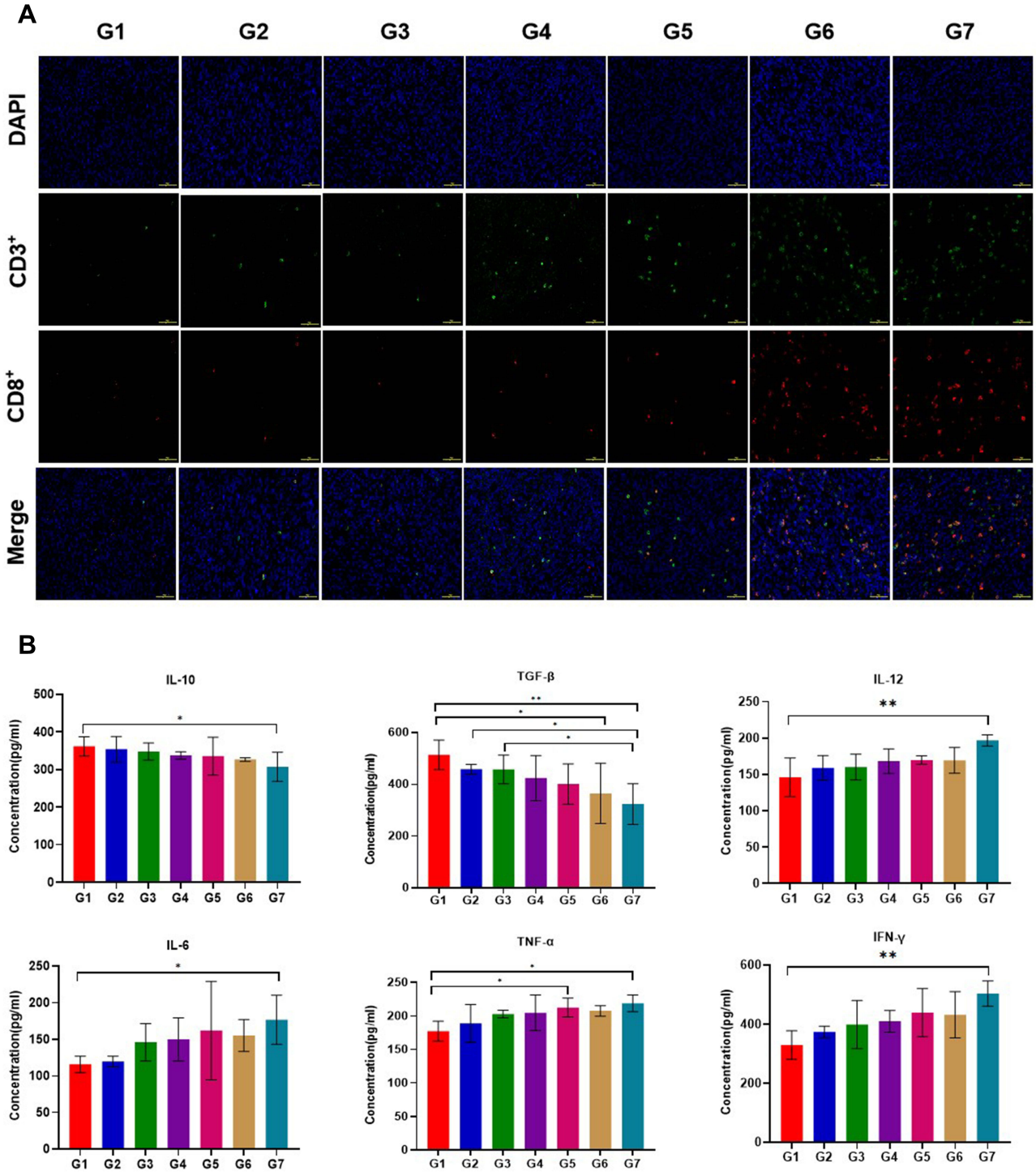

Figure 7 Effects of PDT/PTT combined with Anti-PD-L1 immunotherapy based on ICG@SANPs-cRGD on T lymphocytes and cytokine tumor tissues. (**A**) Representative immunofluorescence images of tumor tissues stained by $CD3^+$(green) and $CD8^+$(red) in different groups (scale bar = 50μm). (**B**) Effects of PDT/PTT combined with Anti-PD-L1 immunotherapy based on ICG@SANPs-cRGD on cytokine secretion in tumor tissues G1: Control; G2: ICG@SANPs; G3: ICG@SANPs-cRGD; G4: NIR+ICG@SANPs; G5: NIR+ICG@SANPs-cRGD; G6: Anti-PD-L1; G7: NIR+ICG@SANPs-cRGD+Anti-PD-L1. (Data are expressed as means ± SD (n = 3). Statistical significances were calculated via ANOVA, $*p < 0.05$, $**p < 0.01$).

$CD3^+$T cells and $CD8^+$T cells was observed in the other groups. These results indicate that the combination therapy exerts a powerful killing effect on 4T1 tumor cells by recruiting tumor-infiltrating cytotoxic T lymphocytes, enhances the systemic anti-tumor immune response, and achieves the goal of controlling tumor growth.

Cytokines have the functions of regulating innate and adaptive immunity, promoting cell growth and tissue repair, regulating cell proliferation, differentiation and migration, maintaining the stability of internal environment and stimulating inflammatory response, which can promote the growth and invasion of tumor and ultimately affect the prognosis of tumor patients.[57,58] As shown in Figure 7B, compared with the control group, the expressions of pro-inflammatory factors IL-6, IL-12, TNF-α and IFN-γ were increased in mice treated with ICG@SANPs-cRGD+Anti-PD-L1, while the expressions of anti-inflammatory factors TGF-β and IL-10 were decreased. Compared with other treatment groups, NIR+ICG@SANPs-cRGD+Anti-PD-L1 could up-regulate the secretion of IL-6, IL-12, TNF-α and IFN-γ, and down-regulate the secretion of immunosuppressive factors TGF-β and IL-10. These results indicate that ICG@SANPs-cRGD-based PDT/PTT combined with immune checkpoint blocker Anti-PD-L1 therapy can effectively improve the tumor microenvironment, effectively activate and enhance the body's positive immune response against tumor, and inhibit the immunosuppressive response promoting tumor growth in the immune microenvironment. The combination therapy plays a good role in the treatment of 4T1 breast cancer by affecting the secretion of cytokines.

In the study of the mechanism of the activation of the immune system by combination therapy, it was found that ICG@SANPs-cRGD mediated PDT/PTT combined with Anti-PD-L1 therapy realized the combination of ICD and ICB by affecting the expression of relevant immune indicators, activated the immune response of the body, and exerted strong anti-tumor potential.

Conclusion

In this study, ICG@SANPs-cRGD multifunctional nanoparticles were successfully prepared, and the combination of tumor phototherapy and immunotherapy was realized by enhancing the effect of PTT/PDT combined with Anti-PD-L1 immunotherapy in the treatment of breast cancer. The results of in vitro and in vivo experiments showed that ICG@SANPs-cRGD enhanced the effect of PTT/PDT under NIR irradiation, effectively inhibited the proliferation of 4T1 tumor cells, and promoted the apoptosis of 4T1 cells. ROS were generated by PDT stimulation and induced cell immunogenic death. PTT also played a good role in killing tumor cells through photothermal conversion. In addition, ICG@SANPs-cRGD can effectively target tumor tissues when treated in vivo. Due to EPR effect and active targeting, it shows good FL/MRI dual-mode imaging ability, thus effectively inhibiting tumor growth under NIR light irradiation. More importantly, ICG@SANPs-cRGD-mediated PTT/PDT induced the immunogenic environment of the tumor and sensitized the tumor to Anti-PD-L1 immune checkpoint blockade therapy, realizing the combined treatment of ICD and ICB in breast cancer. Therefore, the combination therapy of PTT/PDT and Anti-PD-L1 based on ICG@SANPs-cRGD not only showed a good therapeutic effect on the primary tumor but also inhibited the distant metastatic tumor by generating a systemic anti-tumor immune response. In conclusion, this study is helpful to realize the integration of multimodal tumor therapy and diagnosis and treatment, provides a safe and effective alternative strategy for breast cancer treatment, and provides a theoretical reference for the combination therapy of phototherapy and immune activation and also hope that ICG@SANPs-cRGD can be used as a potentially effective nanomedicine for the diagnosis and treatment of clinical breast cancer in the future.

Acknowledgments

This work was supported by the National Natural Science Foundation of China Regional Fund (82160341), Guangxi Natural Science Foundation Key Project (2022GXNSFDA035060) the Basic Research Ability Improvement Project for Young and Middle-aged Teachers in Guangxi Colleges and Universities (2022KY0116), and the Youth Program of Scientific Research Foundation of Guangxi Medical University Cancer Hospital (Yuan Qing no. 2021-09).

Author Contributions

All authors made a significant contribution to the work reported, whether that is in the conception, study design, execution, acquisition of data, analysis and interpretation, or in all these areas; took part in drafting, revising or critically reviewing the article; gave final approval of the version to be published; have agreed on the journal to which the article has been submitted; and agree to be accountable for all aspects of the work.

Disclosure

The authors declare that they have no competing interests.

References

1. Siegel RL, Miller KD, Jemal A. Cancer statistics, 2020. *CA Cancer J Clin*. 2020;70(1):7–30. doi:10.3322/caac.21590
2. Hao Y, Chen Y, He X, et al. Near-infrared responsive 5-fluorouracil and indocyanine green loaded MPEG-PCL nanoparticle integrated with dissolvable microneedle for skin cancer therapy. *Bioact Mater*. 2020;5(3):542–552. doi:10.1016/j.bioactmat.2020.04.002
3. Shi S, Vissapragada R, Abi Jaoude J, et al. Evolving role of biomaterials in diagnostic and therapeutic radiation oncology. *Bioact Mater*. 2020;5(2):233–240. doi:10.1016/j.bioactmat.2020.01.011
4. Dodwell D, Jauhari Y, Gathani T, et al. Treatment variation in early breast cancer in the UK. *BMJ*. 2020;371:m4237. doi:10.1136/bmj.m4237
5. Li X, Lovell JF, Yoon J, Chen X. Clinical development and potential of photothermal and photodynamic therapies for cancer. *Nat Rev Clin Oncol*. 2020;17(11):657–674. doi:10.1038/s41571-020-0410-2
6. Qi T, Chen B, Wang Z, et al. A pH-Activatable nanoparticle for dual-stage precisely mitochondria-targeted photodynamic anticancer therapy. *Biomaterials*. 2019;213:119219. doi:10.1016/j.biomaterials.2019.05.030
7. Wang H, Mao X. Evaluation of the Efficacy of Neoadjuvant Chemotherapy for Breast Cancer. *Drug Des Devel Ther*. 2020;14:2423–2433. doi:10.2147/DDDT.S253961
8. Ma Q, Sun X, Wang W, et al. Diketopyrrolopyrrole-derived organic small molecular dyes for tumor phototheranostics. *Chine Chem Lett*. 2022;33(4):12. doi:10.1016/j.cclet.2021.10.054
9. Qu XY, Hong Y, Cai H, et al. Promoted intramolecular photoinduced-electron transfer for multi-mode imaging-guided cancer photothermal therapy. *Rare Metals*. 2022;41(1):11. doi:10.1007/s12598-021-01795-0
10. Xiong R, Hua D, Van Hoeck J, et al. Photothermal nanofibres enable safe engineering of therapeutic cells. *Nat Nanotechnol*. 2021;16(11):1281–1291. doi:10.1038/s41565-021-00976-3
11. Xiong R, Xu RX, Huang C, De Smedt S, Braeckmans K. Stimuli-responsive nanobubbles for biomedical applications. *Chem Soc Rev*. 2021;50(9):5746–5776. doi:10.1039/C9CS00839J
12. Yang X, Wang D, Shi Y, et al. Black Phosphorus Nanosheets Immobilizing Ce6 for Imaging-Guided Photothermal/Photodynamic Cancer Therapy. *ACS Appl Mater Interfaces*. 2018;10(15):12431–12440. doi:10.1021/acsami.8b00276
13. Zhang A, Li A, Zhao W, Liu J. Recent Advances in Functional Polymer Decorated Two-Dimensional Transition-Metal Dichalcogenides Nanomaterials for Chemo-Photothermal Therapy. *Chemistry*. 2018;24(17):4215–4227. doi:10.1002/chem.201704197
14. Sun Y, Zhao D, Wang G, et al. Recent progress of hypoxia-modulated multifunctional nanomedicines to enhance photodynamic therapy: opportunities, challenges, and future development. *Acta Pharm Sin B*. 2020;10(8):1382–1396. doi:10.1016/j.apsb.2020.01.004
15. Zhang Y, Wan Y, Chen Y, Blum NT, Lin J, Huang P. Ultrasound-Enhanced Chemo-Photodynamic Combination Therapy by Using Albumin "Nanoglue"-Based Nanotheranostics. *ACS Nano*. 2020;14(5):5560–5569. doi:10.1021/acsnano.9b09827
16. Zhao C, Tong Y, Li X, et al. Photosensitive Nanoparticles Combining Vascular-Independent Intratumor Distribution and On-Demand Oxygen-Depot Delivery for Enhanced Cancer Photodynamic Therapy. *Small*. 2018;14(12):e1703045. doi:10.1002/smll.201703045
17. Wang H, Pan X, Wang X, et al. Degradable Carbon-Silica Nanocomposite with Immunoadjuvant Property for Dual-Modality Photothermal/Photodynamic Therapy. *ACS Nano*. 2020;14(3):2847–2859. doi:10.1021/acsnano.9b06168
18. Lu H, Zada S, Tang S, et al. Artificial photoactive chlorophyll conjugated vanadium carbide nanostructure for synergistic photothermal/photodynamic therapy of cancer. *J Nanobiotechnology*. 2022;20(1):121. doi:10.1186/s12951-022-01331-x
19. Cao Y, Wang K, Zhu P, et al. A near-infrared triggered upconversion/MoS(2) nanoplatform for tumour-targeted chemo-photodynamic combination therapy. *Colloids Surf B Biointerfaces*. 2022;213:112393. doi:10.1016/j.colsurfb.2022.112393
20. Masugi Y, Nishihara R, Yang J, et al. Tumour CD274 (PD-L1) expression and T cells in colorectal cancer. *Gut*. 2017;66(8):1463–1473. doi:10.1136/gutjnl-2016-311421
21. Bao R, Wang Y, Lai J, et al. Enhancing Anti-PD-1/PD-L1 Immune Checkpoint Inhibitory Cancer Therapy by CD276-Targeted Photodynamic Ablation of Tumor Cells and Tumor Vasculature. *Mol Pharm*. 2019;16(1):339–348. doi:10.1021/acs.molpharmaceut.8b00997
22. Ugai T, Zhao M, Shimizu T, et al. Association of PIK3CA mutation and PTEN loss with expression of CD274 (PD-L1) in colorectal carcinoma. *Oncoimmunology*. 2021;10(1):1956173. doi:10.1080/2162402X.2021.1956173
23. Schmid P, Rugo HS, Adams S, et al. Atezolizumab plus nab-paclitaxel as first-line treatment for unresectable, locally advanced or metastatic triple-negative breast cancer (IMpassion130): updated efficacy results from a randomised, double-blind, placebo-controlled, Phase 3 trial. *Lancet Oncol*. 2020;21(1):44–59. doi:10.1016/S1470-2045(19)30689-8
24. Thoma C. Bladder cancer: mechanisms of anti-PDL1 resistance. *Nat Rev Urol*. 2018;15(4):201. doi:10.1038/nrurol.2018.28
25. Herbst RS, Giaccone G, De Marinis F, et al. Atezolizumab for First-Line Treatment of PD-L1-Selected Patients with NSCLC. *N Engl J Med*. 2020;383(14):1328–1339. doi:10.1056/NEJMoa1917346
26. Li Q, Kartikowati CW, Horie S, Ogi T, Iwaki T, Okuyama K. Correlation between particle size/domain structure and magnetic properties of highly crystalline Fe(3)O(4) nanoparticles. *Sci Rep*. 2017;7(1):9894. doi:10.1038/s41598-017-09897-5
27. Yoo D, Lee JH, Shin TH, Cheon J. Theranostic magnetic nanoparticles. *Acc Chem Res*. 2011;44(10):863–874. doi:10.1021/ar200085c
28. Lee JH, Jang JT, Choi JS, et al. Exchange-coupled magnetic nanoparticles for efficient heat induction. *Nat Nanotechnol*. 2011;6(7):418–422. doi:10.1038/nnano.2011.95
29. Roca AG, Marco JF, Morales MDP, Serna CJ. Effect of Nature and Particle Size on Properties of Uniform Magnetite and Maghemite Nanoparticles. *J Phys Chem C*. 2007;111(50):18577–18584. doi:10.1021/jp075133m
30. Luo T, Wang D, Liu L, et al. Switching Reactive Oxygen Species into Reactive Nitrogen Species by Photocleaved O(2) -Released Nanoplatforms Favors Hypoxic Tumor Repression. *Adv Sci*. 2021;8(19):e2101065. doi:10.1002/advs.202101065
31. Cai Y, Liang P, Tang Q, et al. Diketopyrrolopyrrole-Triphenylamine Organic Nanoparticles as Multifunctional Reagents for Photoacoustic Imaging-Guided Photodynamic/Photothermal Synergistic Tumor Therapy. *ACS Nano*. 2017;11(1):1054–1063. doi:10.1021/acsnano.6b07927

32. Wang D, Fang W, Huang C, et al. MR imaging guided iron-based nanoenzyme for synergistic Ferroptosis−Starvation therapy in triple negative breast cancer. *Smart Mater Med*. 2022;3:159–167. doi:10.1016/j.smaim.2021.12.008
33. Katsamakas S, Chatzisideri T, Thysiadis S, Sarli V. RGD-mediated delivery of small-molecule drugs. *Future Med Chem*. 2017;9(6):579–604. doi:10.4155/fmc-2017-0008
34. Song Z, Lin Y, Zhang X, et al. Cyclic RGD peptide-modified liposomal drug delivery system for targeted oral apatinib administration: enhanced cellular uptake and improved therapeutic effects. *Int J Nanomedicine*. 2017;12:1941–1958. doi:10.2147/IJN.S125573
35. Peng HS, Chiu DT. Soft fluorescent nanomaterials for biological and biomedical imaging. *Chem Soc Rev*. 2015;44(14):4699–4722. doi:10.1039/C4CS00294F
36. Luo Y, Yang J, Yan Y, et al. RGD-functionalized ultrasmall iron oxide nanoparticles for targeted T_1-weighted MR imaging of gliomas. *Nanoscale*. 2015;7(34):14538–14546. doi:10.1039/C5NR04003E
37. Topalian SL, Hodi FS, Brahmer JR, et al. Safety, activity, and immune correlates of anti-PD-1 antibody in cancer. *N Engl J Med*. 2012;366(26):2443–2454. doi:10.1056/NEJMoa1200690
38. Zhang Y, Cheung YK, Ng DKP, Fong WP. Enhancement of innate and adaptive anti-tumor immunity by serum obtained from vascular photodynamic therapy-cured BALB/c mouse. *Cancer Immunol Immunother*. 2021;70(11):3217–3233. doi:10.1007/s00262-021-02917-4
39. Garg AD, Nowis D, Golab J, Agostinis P. Photodynamic therapy: illuminating the road from cell death towards anti-tumour immunity. *Apoptosis*. 2010;15(9):1050–1071. doi:10.1007/s10495-010-0479-7
40. Mroz P, Hashmi JT, Huang YY, Lange N, Hamblin MR. Stimulation of anti-tumor immunity by photodynamic therapy. *Expert Rev Clin Immunol*. 2011;7(1):75–91. doi:10.1586/eci.10.81
41. Guo M, Lv M, Shao Y, Zhang W, Zhao X, Li C. Bax functions as coelomocyte apoptosis regulator in the sea cucumber Apostichopus japonicus. *Dev Comp Immunol*. 2020;102:103490. doi:10.1016/j.dci.2019.103490
42. Qi ZH, Liu YF, Luo SW, Chen CX, Liu Y, Wang WN. Molecular cloning, characterization and expression analysis of tumor suppressor protein p53 from Orange-spotted grouper, Epinephelus coioides in response to temperature stress. *Fish Shellfish Immunol*. 2013;35(5):1466–1476. doi:10.1016/j.fsi.2013.08.011
43. Wang D, Zhou J, Fang W, et al. A multifunctional nanotheranostic agent potentiates erlotinib to EGFR wild-type non-small cell lung cancer. *Bioact Mater*. 2022;13:312–323. doi:10.1016/j.bioactmat.2021.10.046
44. Pena-Blanco A, Garcia-Saez AJ. Bax, Bak and beyond - mitochondrial performance in apoptosis. *FEBS J*. 2018;285(3):416–431. doi:10.1111/febs.14186
45. Davey MG, Hynes SO, Kerin MJ, Miller N, Lowery AJ. Ki-67 as a Prognostic Biomarker in Invasive Breast Cancer. *Cancers*. 2021;13(17):17. doi:10.3390/cancers13174455
46. Li M, Gao Y, Yuan Y, et al. One-Step Formulation of Targeted Aggregation-Induced Emission Dots for Image-Guided Photodynamic Therapy of Cholangiocarcinoma. *ACS Nano*. 2017;11(4):3922–3932. doi:10.1021/acsnano.7b00312
47. Cheng Y, Cheng H, Jiang C, et al. Perfluorocarbon nanoparticles enhance reactive oxygen levels and tumour growth inhibition in photodynamic therapy. *Nat Commun*. 2015;6(1):8785. doi:10.1038/ncomms9785
48. Hwang HS, Shin H, Han J, Na K. Combination of photodynamic therapy (PDT) and anti-tumor immunity in cancer therapy. *J Pharm Investig*. 2018;48(2):143–151. doi:10.1007/s40005-017-0377-x
49. Jing X, Yang F, Shao C, et al. Role of hypoxia in cancer therapy by regulating the tumor microenvironment. *Mol Cancer*. 2019;18(1):157. doi:10.1186/s12943-019-1089-9
50. Lee JW, Bae SH, Jeong JW, Kim SH, Kim KW. Hypoxia-inducible factor (HIF-1)alpha: its protein stability and biological functions. *Exp Mol Med*. 2004;36(1):1–12. doi:10.1038/emm.2004.1
51. Barsoum IB, Smallwood CA, Siemens DR, Graham CH. A mechanism of hypoxia-mediated escape from adaptive immunity in cancer cells. *Cancer Res*. 2014;74(3):665–674. doi:10.1158/0008-5472.CAN-13-0992
52. Iwai Y, Ishida M, Tanaka Y, Okazaki T, Honjo T, Minato N. Involvement of PD-L1 on tumor cells in the escape from host immune system and tumor immunotherapy by PD-L1 blockade. *Proc Natl Acad Sci U S A*. 2002;99(19):12293–12297. doi:10.1073/pnas.192461099
53. Deng H, Zhou Z, Yang W, et al. Endoplasmic Reticulum Targeting to Amplify Immunogenic Cell Death for Cancer Immunotherapy. *Nano Lett*. 2020;20(3):1928–1933. doi:10.1021/acs.nanolett.9b05210
54. Li W, Yang J, Luo L, et al. Targeting photodynamic and photothermal therapy to the endoplasmic reticulum enhances immunogenic cancer cell death. *Nat Commun*. 2019;10(1):3349. doi:10.1038/s41467-019-11269-8
55. Iizuka A, Nonomura C, Ashizawa T, et al. A T-cell-engaging B7-H4/CD3-bispecific Fab-scFv Antibody Targets Human Breast Cancer. *Clin Cancer Res*. 2019;25(9):2925–2934. doi:10.1158/1078-0432.CCR-17-3123
56. Fridman WH, Pages F, Sautes-Fridman C, Galon J. The immune contexture in human tumours: impact on clinical outcome. *Nat Rev Cancer*. 2012;12(4):298–306. doi:10.1038/nrc3245
57. Chow MT, Ozga AJ, Servis RL, et al. Intratumoral Activity of the CXCR3 Chemokine System Is Required for the Efficacy of Anti-PD-1 Therapy. *Immunity*. 2019;50(6):1498–1512 e5. doi:10.1016/j.immuni.2019.04.010
58. Coussens LM, Zitvogel L, Palucka AK. Neutralizing tumor-promoting chronic inflammation: a magic bullet? *Science*. 2013;339(6117):286–291. doi:10.1126/science.1232227